

Diversity of galactic discs at high redshift in cosmological simulations

M2 Internship Report

Author:

Meghna Varma

M2 Space Science and Technology, IRT
Observatoire de Paris-PSL

Supervisor:

Dr. Maxime Trebitsch
LUX, Observatoire de Paris



LUX, Observatoire de Paris
77 Av. Denfert Rochereau, 75014 Paris

ACKNOWLEDGEMENT

I would like to express my deepest gratitude to my supervisor Dr. Maxime Trebitsch, Observatoire de Paris, for his unwavering support, invaluable guidance, and endless patience throughout the journey of completing this project. His expertise, encouragement, and constructive feedback have been instrumental in shaping this work.

I am also grateful to the colleagues of LUX laboratory for their help and support throughout the work.

I would like to extend my sincere thanks to my family, friends and classmates for their constant support and encouragement. Their belief in my abilities has been a source of motivation and inspiration throughout this project.

Contents

1	Introduction	7
1.1	Galaxy formation and evolution: A cosmological context	7
1.2	Galactic morphology	8
1.3	Galactic discs	10
1.4	State of the art	11
1.5	Objective of the study	12
2	Data	14
2.1	Obelisk simulation	14
2.1.1	Stellar modelling and supernovae feedback	15
2.1.2	AGN and black hole modelling	15
2.1.3	Thermodynamics	16
2.2	Sample selection	16
3	Methodology	20
3.1	Morphological decomposition	20
3.2	Fitting	21
3.3	Determination of mass fractions	23
3.4	Kinematic analysis	24
3.4.1	Computing the rotation curve	24
4	Results	26
4.1	Morphological profiling	26
4.1.1	Mass fractions	30
4.1.2	Sersic indices and scale lengths	31
4.2	Kinematic analysis	34
4.2.1	Rotation curves	34
4.2.2	Correlating with morphological profiles and galaxy properties	36
5	Discussion	38
6	Future work	39

List of Figures

1	Flowchart illustrating processes regulating galaxy morphology [Mo et al., 2010]	7
2	Hubble tuning-fork diagram showing the classification of galaxies into elliptical, spiral and irregular morphologies.	9
3	Comparison of HST and JWST observations of galaxies at different redshifts.[Ferreira et al., 2022]	12
4	Snapshot of the central region of Obelisk simulation [Trebitsch et al., 2021]	14

5	Comparison of the Obelisk simulation (lower panel) with the Horizon-AGN simulation(upper panel). Illustrates the increased resolution of Obelisk. [Trebitsch et al., 2021]	15
6	Distribution of stellar mass of galaxies in the sample at redshift $z = 6$	16
7	The distribution of halo in the simulation box. X and Y are thus in box units	17
8	Galaxy 14215.The white dotted circle in (a) represents the half mass radius of the galaxy.	18
9	The star formation rate, mass-averaged metallicity and mass-averaged age of galaxies in the sample. SFR100 is the star formation rate averaged over the last 100 Myr	19
10	Sersic profile for a given central surface density Σ_0 and half-mass radius R_e and different values of the Sersic index n	21
11	Projection of a star onto the galactic disk (in the $\hat{\rho}-\hat{\theta}$ plane).	22
12	Face-on view with annular bins; the highlighted ring is used for computing $\Sigma(R_i)$	22
13	Surface density profile fit for the most massive galaxy in the sample. The black points represent the observed surface density profile, while the solid red line shows the best 2-component fit. The dashed blue line represents the Sersic component of the combined fit, whereas the dotted green line represents that of the exponential component.	26
14	Surface density profile fit for 4 galaxies in the sample. The galaxies are so chosen as to represent the different structural types. The points and lines are same as in figure 13	27
16	Distribution of Sersic index n for the galaxies in the sample. The histogram shows the number of galaxies with a given Sersic index, indicating a range of structural properties.	28
15	Stellar mapping for the galaxies whose surface density profiles are shown in figure 14	29
17	Distribution of disc-to-total ratio (D/T) for galaxies in the sample in each mass bin(left panel). The disc contribution to the total mass of the galaxy with increasing stellar mass(right panel). The shaded regions represent the 25th-75th percentile of the D/T distribution of galaxies. The median D/T value is shown as a solid line	30
18	The exponential scale length R_{exp} of galaxies in the sample as a function of stellar mass M_*	31
19	Scale length variation with disc-to-total ratio (D/T) for galaxies in the sample. The Sersic scale length of galaxies even with a higher D/T ratio is smaller than the exponential scale length.	31
20	32
21	The "effective scale length" of the Sersic component for galaxies with $n \approx 1$ can be approximated to R_{sersic}/β	32

22	Fraction of Sersic scale length and exponential scale length to the R_{95} of the galaxy. The radius enclosing 95% of the stellar mass is a measure of the overall size of the galaxy	33
23	The star formation rate density (Σ_{SFR}) as a function of the disc scale length R_{exp} . The dotted line represents the star formation rate density for a galaxy with a given SFR	34
24	Rotation curves of galaxies in the sample	35
25	The rotation-to-dispersion ratio (V/σ) as a function of distance from the center of mass of the galaxy	36
26	Variation of the rotation-to-dispersion ratio (V/σ) at R_{50} with stellar mass of galaxies in the sample. The shaded region represents a 1σ scatter	37
27	The V/σ at different radii as a function of D/T. The solid line represents the median value of V/σ at each D/T bin, while the shaded region represents the 1σ scatter	37

ABSTRACT

Galactic morphology is fundamental to understanding how galaxies form, interact with their environments and evolve across cosmic time. Recent observations have revealed a surprisingly large population of disc-like galaxies at redshifts as high as $z = 8$, which appears in tension with galaxy formation models. Thus, understanding the structures and evolutionary paths of these early galaxies is crucial for interpreting findings of observatories like JWST. While current simulations have demonstrated that gaseous disc-like structures exist in star-forming galaxies up to $z \sim 5$, their characteristics at earlier times are not yet fully understood. In this study, we aim to explore the presence of discs in cosmological simulations at high redshift to confront the mismatch between the models and the observations.

To investigate this further, we use the high resolution cosmological simulation ‘Obelisk’, to study the morphology of galaxies at $z > 6$. We fit surface density profiles to distinguish between the disc and spheroidal components of the galaxy, employing indicators like bulge-to-total ratio (B/T) and disk-to-total ratio(D/T), which can provide information regarding the formation history of a galaxy. In addition to morphological profiling, we perform a kinematic decomposition to characterize rotationally supported discs. This decomposition identifies cold and warm discs, bulges and stellar halo. A key parameter is the determination of rotation-to-dispersion ratio V/σ that serves as an indicator of the dynamical support within the galaxy, as higher ratios represent disc-like structures. Our study aims to bridge the gap between observations and simulations, enhancing our comprehension of early galaxy formation.

ABSTRACT ¹

La morphologie galactique est essentielle pour comprendre comment les galaxies se forment, interagissent avec leur environnement et évoluent à travers le temps cosmique. Des observations récentes ont mis en évidence une population surprenante de galaxies en forme de disque jusqu'à des redshifts aussi élevés que $z = 8$ ce qui semble en tension avec les modèles de formation galactique. Il est donc crucial de mieux comprendre la structure et les trajectoires évolutives de ces galaxies primitives pour interpréter les résultats d'observatoires tels que le JWST. Bien que les simulations actuelles aient déjà démontré l'existence de structures discales gazeuses dans les galaxies à formation d'étoiles jusqu'à $z \sim 5$, leurs caractéristiques à des époques encore plus précoce restent encore mal comprises. Dans cette étude, nous visons à explorer la présence de disques dans des simulations cosmologiques à haut redshift afin de confronter les modèles aux observations.

Pour approfondir cette question, nous utilisons la simulation cosmologique haute résolution Obelisk pour étudier la morphologie des galaxies à $z > 6$. Nous ajustons les profils de densité de surface afin de distinguer les composantes discales et sphéroïdales des galaxies, en employant des indicateurs tels que le rapport bulbe-sur-total (B/T) et disque-sur-total (D/T), qui renseignent sur l'histoire de formation d'une galaxie. En complément de cette analyse morphologique, nous réalisons une décomposition cinématique permettant de caractériser les en forme de discques soutenus par la rotation. Cette décomposition identifie les disques froids et chauds, les bulbes ainsi que le halo stellaire. Un paramètre clé est le rapport rotation/dispersion V/σ , utilisé comme indicateur de soutien dynamique : des ratios élevés correspondent à des structures de type disque. Notre étude ambitionne ainsi de combler le fossé entre observations et simulations, en enrichissant notre compréhension de la formation des premières galaxies.

1 Introduction

The formation and evolution of galaxies represent one of the most profound and challenging problems in modern astrophysics. While significant efforts have been made, particularly with the emergence of large-scale cosmological simulations and advanced observational facilities, a complete understanding remains incompletely understood.

1.1 Galaxy formation and evolution: A cosmological context

The prevailing theoretical framework for understanding the Universe's large-scale structure and evolution is the Lambda-Cold Dark Matter (Λ CDM) model. This model posits that the Universe is homogeneous and isotropic on large scales, a principle supported by observations such as the Cosmic Microwave Background (CMB) radiation and the distribution of galaxies. Within this cosmological paradigm, the universe's large-scale structure, including the observed distribution of galaxies and galaxy clusters, is predicted to form through the gravitational collapse of small fluctuations in the primordial density field. These initial density variations, though subtle, are critical as they served as the 'seeds' from which all subsequent complex structures ultimately developed.

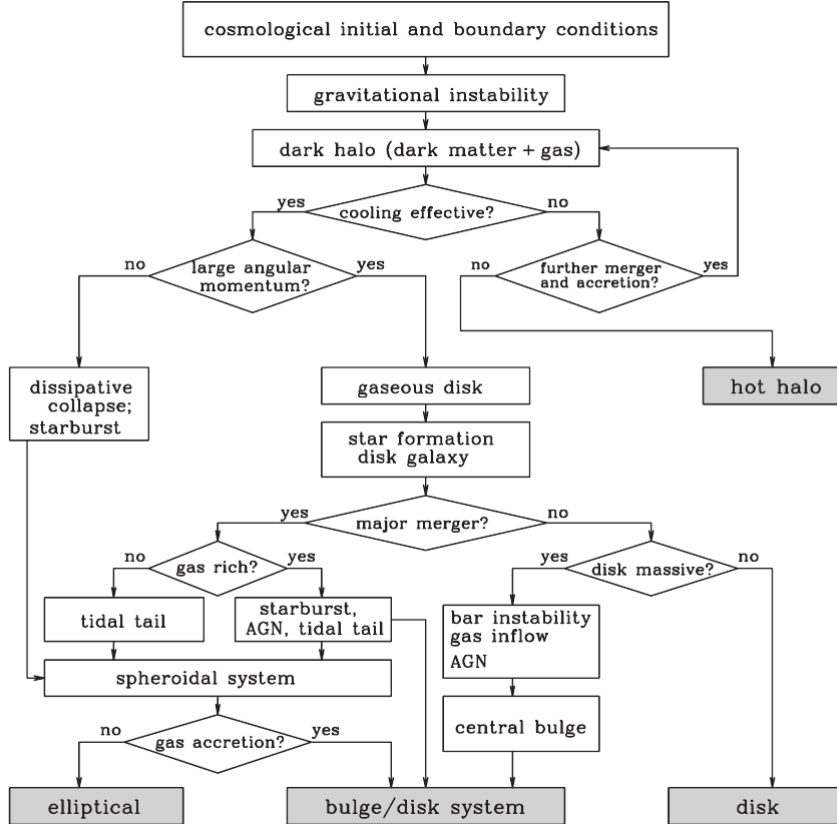


Figure 1: Flowchart illustrating processes regulating galaxy morphology [Mo et al., 2010]

Λ CDM cosmology predicts the formation of galaxies through a hierarchical structure

formation process, where small gravitationally bound structures form first and then merge over cosmic time to create larger ones[[Mo et al., 2010](#)]. This hierarchical growth is a fundamental prediction that shapes the evolutionary pathways of galaxies[[Fall and Efstathiou, 1980](#)]. Initial perturbations in the CDM models contain baryonic gas and dark matter. The dark matter collapses gravitationally to form dark matter halos. Galaxy formation occurs within these haloes, where baryonic matter (primarily hydrogen and helium gas) cools, condenses, and forms stars. The gravitational force must overcome the internal pressure of the gas for it to collapse and form stars. The cooling of gas is facilitated by radiative processes, allowing it to lose energy and settle into the potential wells of dark matter halos. Another major factor that influences the evolution of galaxies is the feedback mechanisms, which regulates the star formation process. Baryonic feedback mechanisms can be in several forms; stellar or from AGN. Stellar feedback that primarily arises from supernova explosions, can heat gas, drive powerful outflows, and regulate star formation. Feedback from AGN or accreting supermassive black hole releases vast amounts of energy, much higher than that in a supernovae feedback and dominates at high halo masses. Triggering an AGN can drive intense outflows that significantly disturb both star formation and the internal dynamics of its host galaxy[[Silk and Rees, 1998](#)]. Furthermore, two or more systems can merge to form another system with different properties. According to the CDM model, a massive halo can be formed from the merging of smaller halos. When two dark matter halos of similar mass merge, violent relaxation rapidly redistributes their orbital energy into internal motions, forming a quasi-equilibrium remnant; any hot gas is shock-heated and then settles back into hydrostatic equilibrium. Their central galaxies coalesce in this process, often triggering intense star formation or AGN activity if substantial cold gas is present. Galaxy surveys reveal numerous instances of galaxies colliding, deforming, and merging to form larger, often morphologically different, galaxies [[Ren et al., 2023](#)][[Fang and Saslaw, 1997](#)]. These interactions can trigger intense bursts of star formation as gas clouds are compressed.

The historical evolution of galaxy formation theories highlights a crucial interplay between initial rapid formation and subsequent gradual assembly. The monolithic collapse model, suggesting a swift, early formation from a single gas cloud, implies a more uniform age distribution of stars within a galaxy. Conversely, the hierarchical model, with its emphasis on mergers of smaller structures, predicts a more diverse stellar population and extended formation timescales. While initially presented as contrasting views, a more complete picture emerges when considering their potential coexistence.

1.2 Galactic morphology

The slow and gradual process of galaxy formation complements the rapid and violent processes of galaxy mergers and interactions, leading to a diverse range of galactic morphologies.

Galaxies exhibit a remarkable diversity in their shapes and structure, which can be often correlated with distinct physical properties and evolutionary pathways. In 1926, Hub-

ble developed a system of classification [Hubble, 1926], which was further developed into the ‘Hubble tuning-fork’ diagram by Hubble and Sandage [1961], which broadly categorizes galaxies into elliptical, spiral, and irregular (or ‘other’) morphologies (refer figure 2). Elliptical galaxies are further subdivided based on their ellipticity, while lenticulars (S0 galaxies) and irregulars also have their own sub-classifications. The classification of spiral galaxies often includes the presence and prominence of a central bar, the tightness of their spiral arms, and the size of their central bulge. Beyond broad Hubble classifications, galaxies are complex systems often composed of several distinct components, such as a star-forming disc, a central spheroidal bulge, a bar, and other substructures. The presence or absence of these components and their characteristics offer valuable clues about the formation histories of their host galaxies.

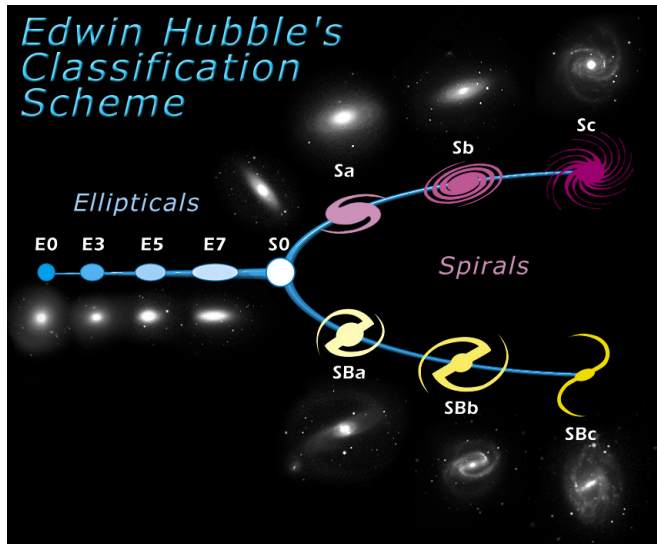


Figure 2: Hubble tuning-fork diagram showing the classification of galaxies into elliptical, spiral and irregular morphologies.

The bulges of typical spiral galaxies, like the Milky Way, are predominantly composed of old stars, suggesting their formation through the primordial collapse of individual gas clouds early in the Universe’s history. However, some bulges, particularly in extremely late-type spiral galaxies, may form almost entirely through secular evolution processes. They are mainly classified into classical bulges, formed by gravitational collapse or hierarchical merging of smaller objects [Toomre, 1977], often before the main disc and pseudo-bulges [Kormendy and Kennicutt, 2004], that are formed from the inflow of gas (and to a lesser extent stars) to the galactic center, followed by subsequent star formation. The morphological, photometric, and kinematical properties of classical bulges are similar to those of elliptical galaxies and pseudo-bulges are typically smaller, have different shapes and kinematics, and often contain a sizable fraction of young stars [Athanassoula and Martinez-Valpuesta, 2007]. The stellar component of galactic discs is generally younger than the stars found in the bulge and halo. Discs are thought to form after the primordial collapse that creates the spheroidal bulge and halo, possibly through the cooling of hot gas contained within the halo of the newly formed galaxy. Discs primarily evolve via star

formation. Many spiral galaxies possess two distinct disc structures: a thick disk and a thin disk.

Decomposition of galaxies into disc and bulge component lays a foundation for categorizing galaxies in the Hubble sequence. In 1948, Gerard de Vaucouleurs showed that elliptical galaxies can be characterized by light distribution, which is now known as the de Vaucouleurs profile[[de Vaucouleurs, 1948](#)]. This was generalised by Sersic in 1963[[Sérsic, 1963](#)] who showed that the surface brightness profile of galaxies can be described by a more general Sersic profile. The Sérsic index describes how concentrated the light is towards the center of the galaxy, with lower values indicating a more diffuse distribution and higher values indicating a more concentrated distribution. The Sérsic profile is given by:

$$I(R) = I_e \exp \left[-b_n \left(\left(\frac{R}{R_e} \right)^{1/n} - 1 \right) \right] \quad (1)$$

A Sersic profile with $n = 4$ describes a de Vaucouleurs profile. Studies have employed this method [[Allen et al., 2006](#)] [[Nedkova et al., 2024](#)] that typically involves two-dimensional (2D) fitting of calibrated images, often using an exponential radial light profile for the disc and either a de Vaucouleurs or exponential profile for the bulge[[Quilley et al., 2025](#)]. Galaxies with ubiquitous bulge and disc components span the various Hubble types, with the bulge-to-total light ratio (B/T) ranging from 0 to 1. The Sérsic index, which describes the concentration of light, also correlates with galaxy morphology and can be used in automated schemes to determine Hubble type. Later, advanced methodologies brought in fitting of bars along with bulge-disc components[[Kormendy, 1979](#)].

1.3 Galactic discs

In the Λ CDM model, disc galaxies (late-type) form from the gas accretion from the circumgalactic medium into the gravitational potential wells of dark matter halos to form a rotating gas disc, followed by an in-situ star formation leading to the formation of rotationally supported stellar discs[[White and Rees, 1978](#)]. The disc contains a large fraction of baryonic mass and angular momentum[[van der Kruit and Freeman, 2011](#)]. Observationally, spiral galaxies exhibit flat rotation curves: after a rapid rise in the inner regions (dominated by baryonic mass), the orbital velocity remains approximately constant out to large radii, well beyond the visible disk. This implies the presence of an extended dark matter halo that dominates the gravitational potential in outer regions. Many discs show extended HI warps and star formation at large radii, and their stellar abundance gradients tend to flatten or even invert in the outskirts. Nearby spiral galaxies have a cold thin disc consisting of young stars, embedded in a thick disc.

However, cosmological hydrodynamical simulations historically suffered an 'angular momentum problem', where baryons lost too much angular momentum and produced overly compact, bulge dominated galaxies with unrealistic rotation curves[[Navarro and Steinmetz, 2000](#)]. A key breakthrough was the realization that strong feedback from super-

novae, radiation etc can eject low-angular momentum gas, allowing gas to form a large disc.[[Governato et al., 2010](#)][[Agertz et al., 2011](#)]. During this hierarchical assembly, discs can form early. For example, surveys find many $z \sim 2$ galaxies already contain rotationally supported stellar discs, although they are still turbulent and not fully settled.[[van der Kruit and Freeman, 2011](#)].

1.4 State of the art

High redshift surveys using HST, AO-fed IFUs, and ALMA have revealed that many $z > 1$ star-forming galaxies are rotationally supported discs.[[Nelson et al., 2013](#)][[Wisnioski et al., 2019](#)][[Parlanti et al., 2023](#)]. By $z \sim 2$ (the ‘cosmic noon’), large star-forming discs were common, yet they are clumpier and thicker than today’s discs. For instance [Smit et al. \[2018\]](#) report ALMA [C-II] observations of two $z \simeq 6.85$ galaxies with resolved velocity gradients indicating rotation; they find these early discs to be ‘turbulent, yet rotation-dominated’ and dynamically akin to $z \sim 2$ H α -emitting discs. In general, disk thickness and dispersion increase with redshift as gas fractions rise. The emerging picture is one of violent disk instabilities (VDIs): gas-rich disks rapidly form massive clumps via gravitational instability, even when the average Toomre Q is above unity[[Toomre, 1964](#)]. Such instabilities can build up bulges and thick disks over time.[[Bournaud et al., 2007](#)].

Key observational advances like the ones mentioned above have transformed our view of disk galaxies. Observations over the last decade increasingly show that many star-forming galaxies at $z \sim 2 - 10$ exhibit kinematics and structure indicative of disk-like, rotation-supported systems. In addition, recent ALMA surveys [[Le Fèvre et al., 2020](#)][[Parlanti et al., 2023](#)] find a subset of $z \gtrsim 5$ galaxies whose [C-II] kinematics are consistent with rotating, though highly turbulent, disks. These ALMA results indicate that by $z \sim 5 - 7$ a non-negligible fraction of massive galaxies already host disky, rotating gas reservoirs, even if velocity dispersions are several times higher than in local disks. High-resolution imaging (HST, adaptive optics) reveals that many high- z galaxies have elongated or clumpy light profiles suggestive of thick disks or chains (though interpretation is complicated by clumps). Where combined with kinematics, these morphologies often correlate with rotation. The emergence of JWST enhanced our observational capacities. It extends the redshift range in which we can observe galaxies in the rest-frame optical light, allowing morphological analysis to be performed upto as high as $z \sim 9$. For example, [Ferreira et al. \[2022\]](#)[Ferreira et al. \[2023\]](#) used JWST in CEERS to analyze 247 galaxies across $1 \leq z \leq 3$, finding a high fraction of disk breaks, spiral arms, and bar features traditionally associated with mature disks. [Danhaine et al. \[2025\]](#) used JWST/NIRCam grism spectroscopy (JADES, FRESCO) to probe ionized gas kinematics in 272 galaxies at $3.9 \leq z \leq 6.5$.

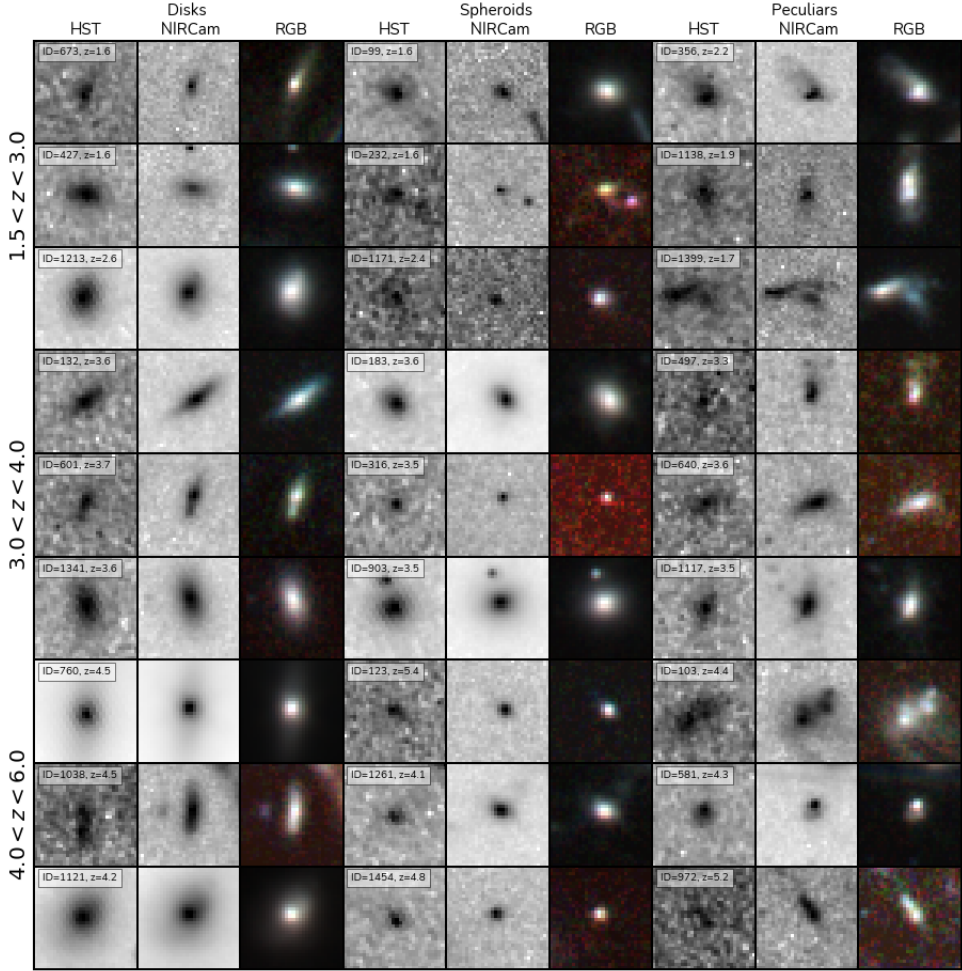


Figure 3: Comparison of HST and JWST observations of galaxies at different redshifts. [Ferreira et al., 2022]

In the context of simulations, modern cosmological simulations confirm the observations upto an extent of $z \sim 5$. The IllustrisTNG [Pillepich et al., 2019] show that most-star forming galaxies at $10^9 - 10^{11} M_{\odot}$ show substantial rotational support. This study demonstrate that in TNG50 the gas in early galaxies arranges into disk-like shapes at all epochs, with $V_{\text{max}}/\sigma \gtrsim 2-3$ up to $z \sim 5$. Zoom-in FIRE(Feedback in Realistic environment [Gurvich et al., 2022]) simulations show somewhat later disk settling for Milky-Way-mass progenitors. In FIRE-2 runs of MW-like halos, the interstellar medium remains dispersion-dominated and bursty at $z \gtrsim 1$, with stable rotational disks only emerging around $z \sim 0.5-1$. This study finds that rotational support is subdominant at early times in FIRE; disks form rapidly once star formation steadies.

1.5 Objective of the study

While modern cosmological simulations have made significant progress in understanding the presence and formation of discs at high redshift, the maximum redshift at which discs are reliably identified is still limited to $z \sim 5$. This study aims to extend the analysis of disc galaxies to a higher redshift, $z = 6$, using the high resolution cosmological simulation Obelisk, which will be discussed in the next section. The goal of this study is to identify

the diversity of disc-like structures in galaxies at this redshift thereby trying to bridge the gap between observational evidences and current models of galaxy formation. This thesis is organised as follows: Section 2 explains the data used for the analysis, section 3 explains the methods employed to identify the structural properties and kinematics of the galaxies, section 4 and 5 presents the findings and discusses the interpretation respectively. Section 6 mentions an outline of future scope of this work.

2 Data

In this section, I describe the data used to analyse the structural properties of galaxies and their kinematics at a high redshift. In addition, I outline the properties of the galaxies in the sample.

2.1 Obelisk simulation

This study utilizes data from the high resolution ($\Delta x = 35\text{pc}$) cosmological radiation-hydrodynamics simulation Obelisk[[Treibitsch et al., 2021](#)]. The simulation, a subvolume and a resimulation of the Horizon-AGN simulation (refer Figure 5) at a much higher resolution down to $z \simeq 3.5$ [[Dubois et al., 2016](#)], is designed to explore the formation and co-evolution of galaxies in an environment that favours the growth of black holes. It assumes a ΛCDM cosmology with WMAP-7 parameters[[Komatsu et al., 2011](#)]: Hubble constant $H_0 = 70.4\text{km}\text{s}^{-1}\text{Mpc}^{-1}$, total matter density $\Omega_m = 0.272$, dark energy density $\Omega_\Lambda = 0.728$, baryon density $\Omega_b = 0.0455$, amplitude of matter power spectrum $\sigma_8 = 0.81$ and scalar spectral index $n_s = 0.967$; with a cosmological volume of side $L_{box} = 100h^{-1}\text{cMpc}$ and periodic boundary conditions.

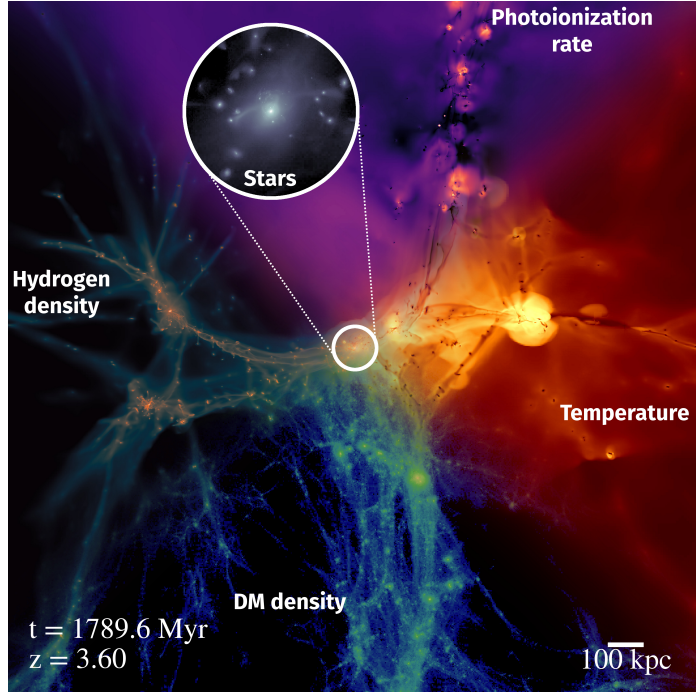


Figure 4: Snapshot of the central region of Obelisk simulation [[Treibitsch et al., 2021](#)]

The simulation is based on `RAMSES-RT` [[Teyssier, 2002](#)], a radiative transfer hydrodynamical code which is an extension of the adaptive mesh refinement code `RAMSES`, and follows the evolution of stars, gas, dark matter and black holes through hydrodynamics, radiative transfer and gravity. The galaxies and haloes are identified using the `ADAPTAHOP` halo finder[[Aubert et al., 2004](#)][[Tweed et al., 2009](#)]. Galaxies are considered as all the stellar particles in the substructure and only galaxies with more than 100 star particles are considered for the analysis.

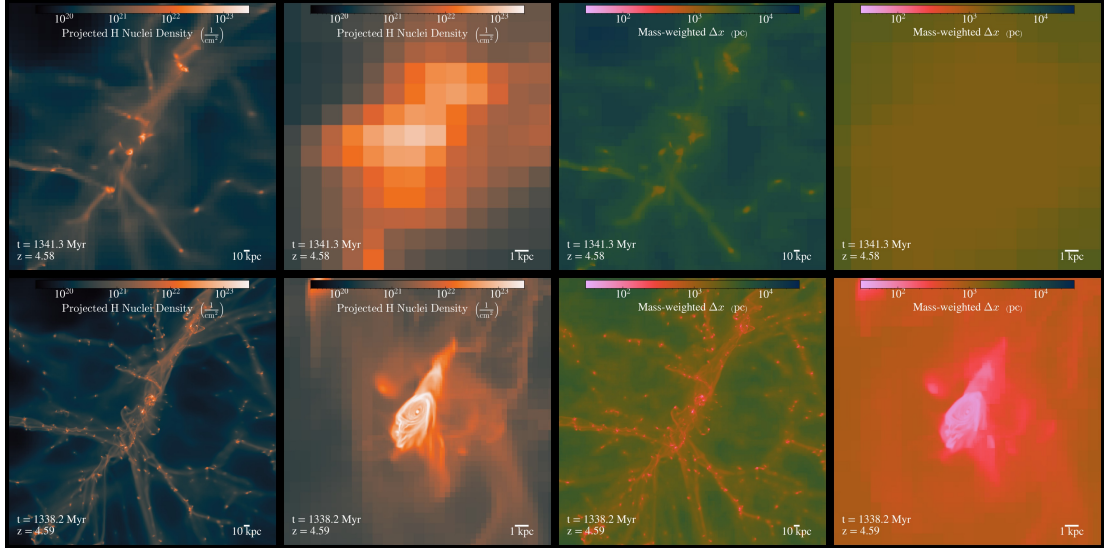


Figure 5: Comparison of the Obelisk simulation (lower panel) with the Horizon-AGN simulation(upper panel). Illustrates the increased resolution of Obelisk. [Trebitsch et al., 2021]

2.1.1 Stellar modelling and supernovae feedback

The simulation measures the global properties of total structure as well as properties corresponding separately to stars, gas and dark matter. Stars are modelled as particles with $m_* \sim 10^4 M_\odot$ formed in a dense and turbulent Interstellar Medium (ISM), assuming an initial mass function between 0.1 and $100 M_\odot$. These stars form in gas cells whose mass density is more than the ISM density $5 H cm^{-3}$ and has a Mach number(ratio of turbulent velocity to sound speed) $\mathcal{M} \geq 2$. In the high resolution region, dark matter particles have a mass of $1.2 \times 10^6 M_\odot$. Each star is assumed to explode at $t_{SN} = 5$ Myr after formation. A fraction, $\eta_{SN} = 0.2$, of the initial stellar population is ejected as supernovae material, including mass, energy as well as momentum, releasing 10^{51} erg per SN.

2.1.2 AGN and black hole modelling

Modelled as sink particles with initial mass $M_{,0} = 3 \times 10^4 M_\odot$ that accrete gas and are allowed to eject energy and momentum into its environment, black holes(BH) form in the cells with a star and gas density greater than $100 H cm^{-3}$ and where the gas is Jeans-unstable (this makes the gas collapse gravitationally to form stars). The BH then grows through BH-BH mergers and gas accretion. The simulation also includes a dual-mode feedback model for AGN. Below an Eddington ratio of 0.01, the AGN is assumed to be in a radiatively inefficient mode ('radio' mode), where it ejects energy and momentum into the surrounding gas in the form of jets [Volonteri et al., 2025]. For a higher Eddington ratio, the AGN is said to be in 'quasar' mode, where the feedback is isotropic thermal energy.

2.1.3 Thermodynamics

For the gas, an ideal gas equation of state for a monoatomic gas is assumed, with an adiabatic index of $\gamma = 5/3$. Cells are refined up to a smallest size of 35 pc if its mass exceeds 8 times the mass resolution. It incorporates comprehensive cooling and heating processes that bring the gas temperature down to as low as 50K with non-thermal equilibrium thermochemistry for hydrogen and helium and also includes metal-driven cooling by assuming their ionization states are in equilibrium with a UV background spectrum.

2.2 Sample selection

In this study, I focus on the galaxies at redshift $z = 6$. Figure 6 shows the stellar mass distribution of galaxies in the sample. I select galaxies with a stellar mass greater than $10^7 M_\odot$. At lower masses, galaxies are typically represented by fewer star particles, which limits the reliability of derived physical quantities such as stellar kinematics or morphology. This cut off on the stellar mass ensures that the sample contains galaxies with sufficient resolution. The sample consists of 1391 galaxies with a stellar mass greater than $10^7 M_\odot$ at redshift $z = 6$.

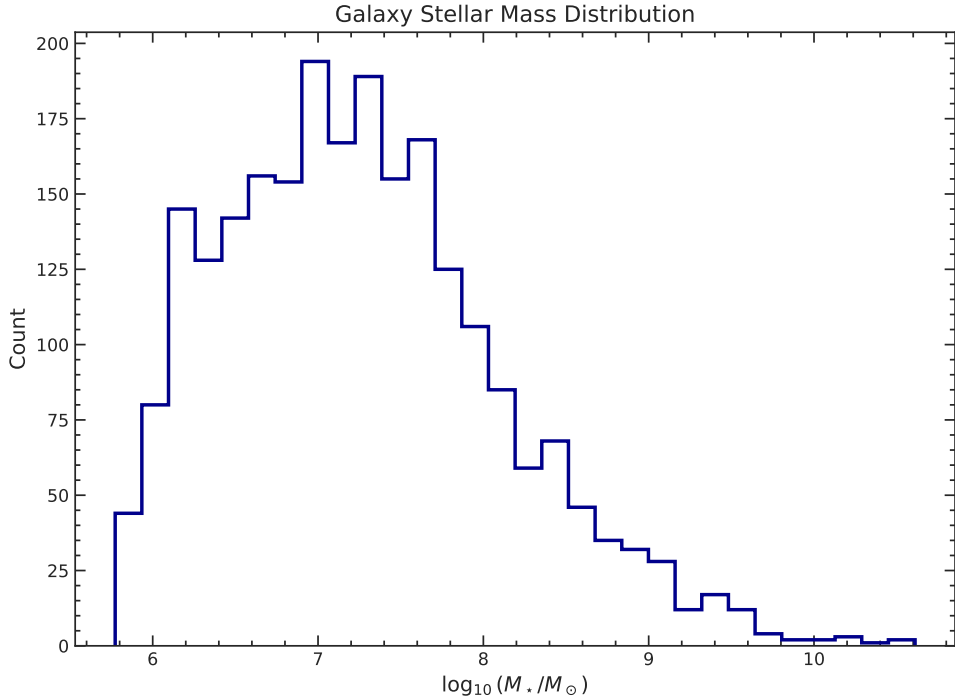


Figure 6: Distribution of stellar mass of galaxies in the sample at redshift $z = 6$

The main data catalogue contains the information on halo properties. Each halo is uniquely identified by an ID and is characterized by a hierarchical level, indicating whether it's a parent-level halo or a substructure. The dataset also encodes information about the structure of halos, such as their virial properties (mass, radius, temperature), dynamical

state (velocity dispersion, kinetic and potential energy), and shape (derived from the inertial tensor).

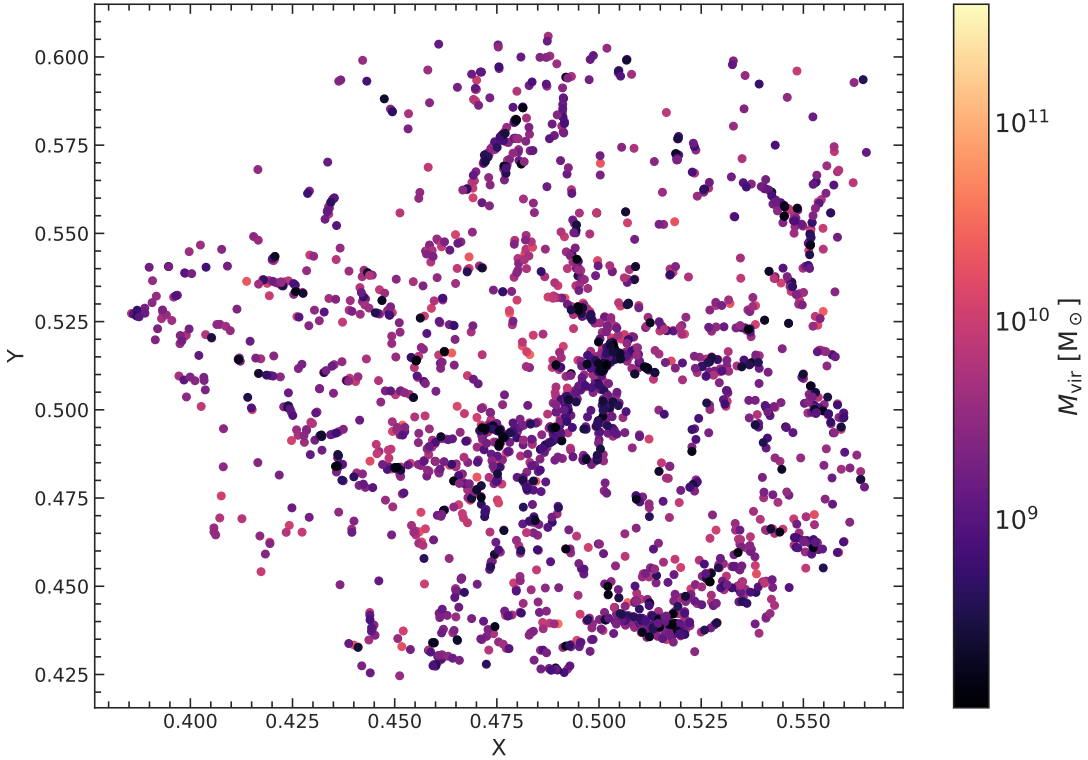
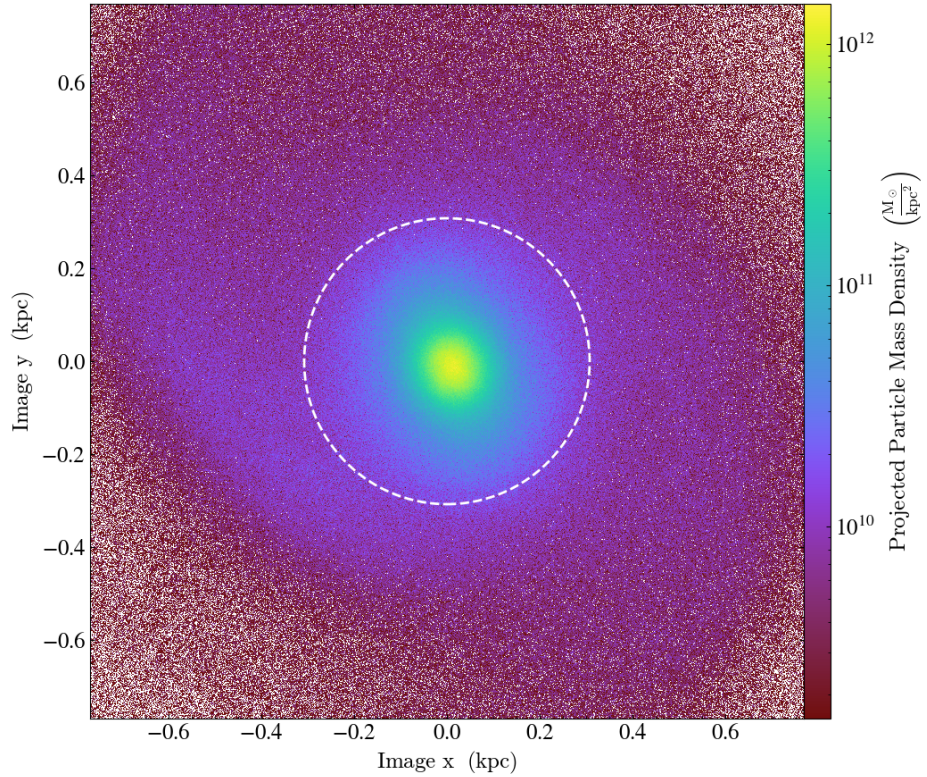


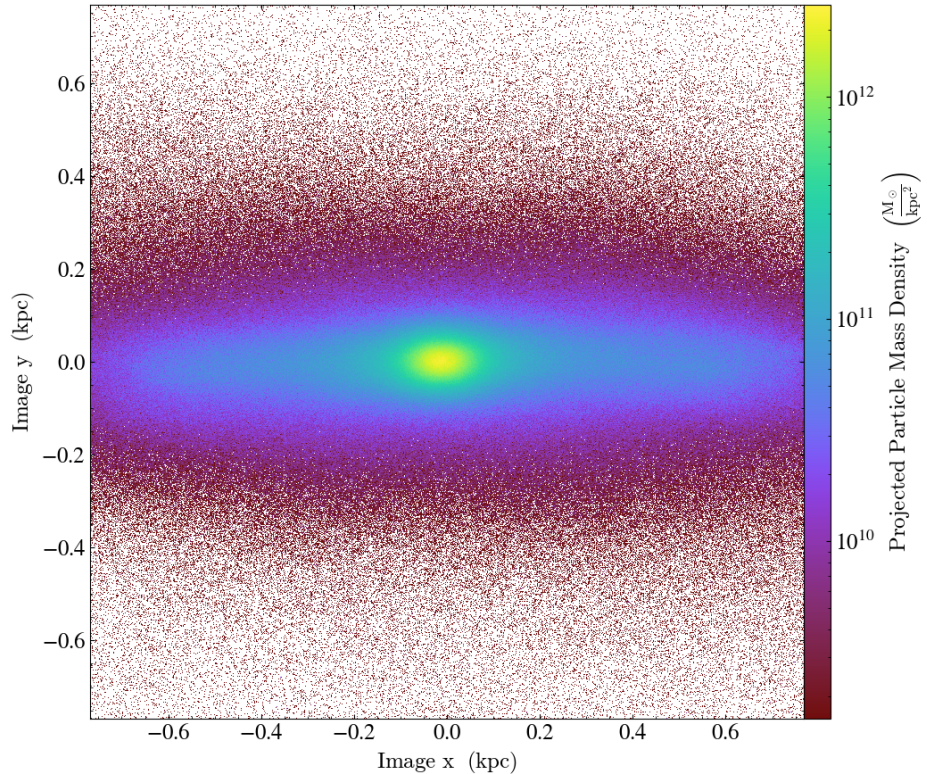
Figure 7: The distribution of halo in the simulation box. X and Y are thus in box units

The main catalogue also contains basic galaxy information including their positions, velocities, mass, angular momentum and age along with information on its sizes, baryon content, kinematical information, environment and the presence of black holes. Figure 9 shows the properties of galaxies in the sample analysed in terms of their stellar mass, star formation rate, metallicity and age. It indicates a more continuous star formation in massive systems, with increasing metallicity. The data remains consistent with the current knowledge in galaxy evolution, wherein low mass galaxies at high redshift are typically metal poor, due to shallow potential wells leading to a loss of a significant fraction of their gas and metals. Massive galaxies, with a deeper potential well prevent metals from escaping and enables accretion of vast amount of cold gas, leading to higher metallicity and star formation rates.

The most massive galaxy in the simulation has a stellar mass of $4.0855e + 10 M_{\odot}$ and a total gas mass of $2.201e + 10 M_{\odot}$ in the halo. Figure 8 shows the maps of the stellar distribution of this galaxy.



(a) Face-on view



(b) Edge-on view

Figure 8: Galaxy 14215. The white dotted circle in (a) represents the half mass radius of the galaxy.

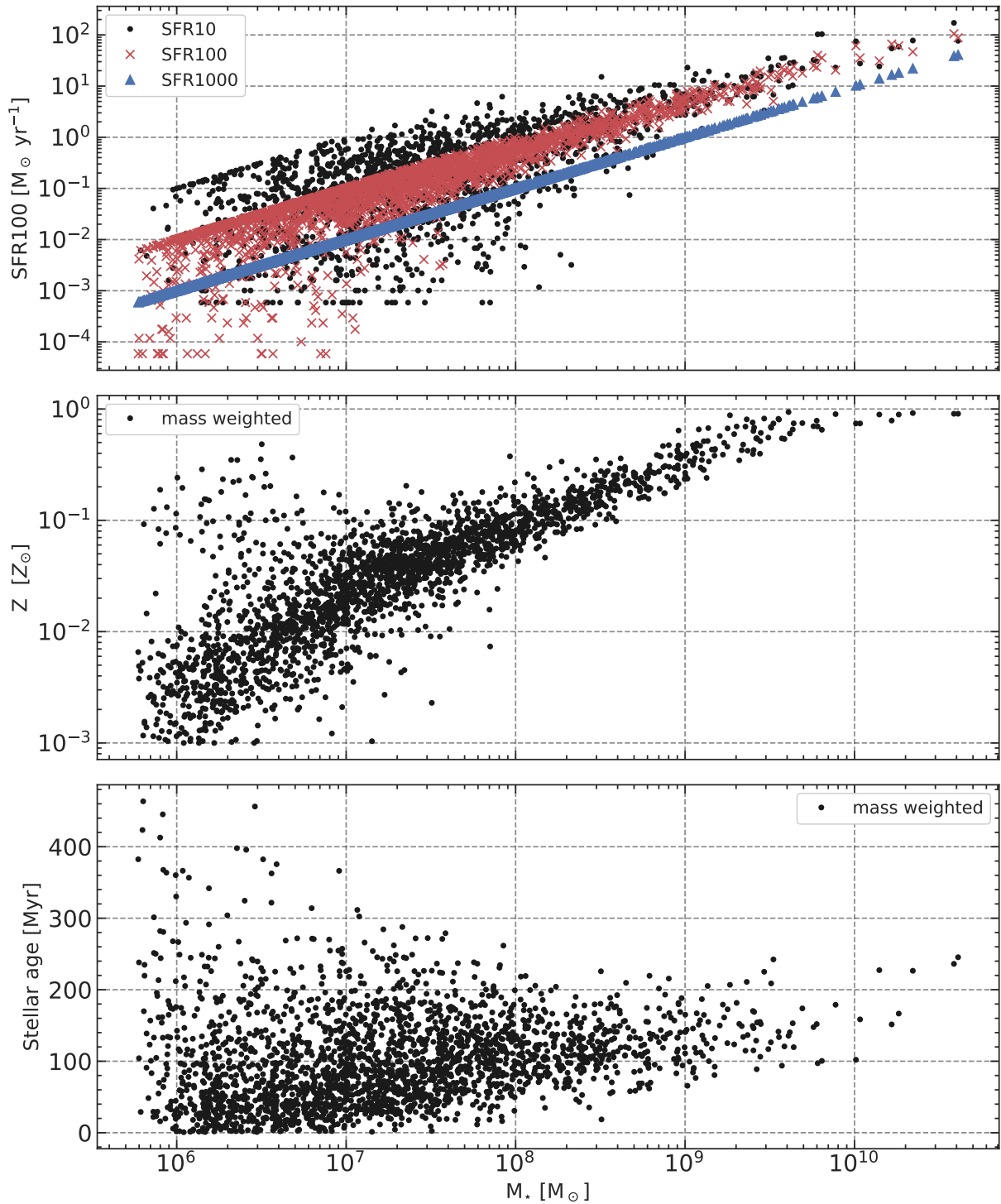


Figure 9: The star formation rate, mass-averaged metallicity and mass-averaged age of galaxies in the sample. SFR100 is the star formation rate averaged over the last 100 Myr

3 Methodology

In this study, I employ the two-component analysis- combining bulge-disc decomposition and a kinematic analysis- to characterize the structural and dynamical properties of the galaxies (the two-component decomposition is discussed in section 1).

3.1 Morphological decomposition

In this model, the bulge and disc components are constrained to share a common center of mass. This central alignment ensures a physically consistent representation of the galaxy's structure. The stars are projected onto a plane perpendicular to the angular momentum (\vec{L}) of the galaxy. For this decomposition, one usually fits $\Sigma(R)$ with the sum of a Sersic profile for the bulge [Sersic, 1968][Graham and Driver, 2005] and an exponential profile for the disc.[Freeman, 1970]

The discs of galaxies can be modelled as an infinitely thin disc with an exponential surface density profile, with the distribution described by

$$\Sigma(R) = \Sigma_0 \exp\left(\frac{-R}{R_d}\right) \quad (2)$$

where R_d is the disc scale length and $\Sigma(0)$ is the central surface density. The scale length describes the radius at which the central surface density decreases by a factor of e. For a purely exponential disc, the radius enclosing half of the total mass of the galaxy, half-mass radius (R_e) $\simeq 1.67R_d$.

The Sersic profile (or the $R^{1/n}$ profile) describes the surface density $\Sigma(R)$ as a function of radius R from the galaxy center as

$$\Sigma(R) = \Sigma_0 \exp\left[-\beta_n \left\{ \left(\frac{R}{R_e}\right)^{1/n} \right\}\right] = \Sigma(R_e) \exp\left[-\beta_n \left\{ \left(\frac{R}{R_e}\right)^{1/n} - 1 \right\}\right] \quad (3)$$

where n is called the Sersic index which determines the concentration and shape of the galaxy's profile. Lower values of n (for instance, $n \approx 1$) would correspond to disc-like structures with exponential profiles. The value of β_n , which follows from the definition of R_e can be approximated as $\beta_n = 2n - 0.324$ for ($n \geq 1$).

This approach might be not entirely straightforward since real galaxies often exhibit complex structures that deviate from this simple model. For instance, surface density profiles may show features such as bars or spiral arms which may not be accounted in the basic bulge-disc decomposition. However, this approach remains a fundamental tool in the structure analysis of galaxies due to the ability to classify morphology quantitatively, simplify complex structures, facilitate scaling relations and provide insights into galaxy formation.

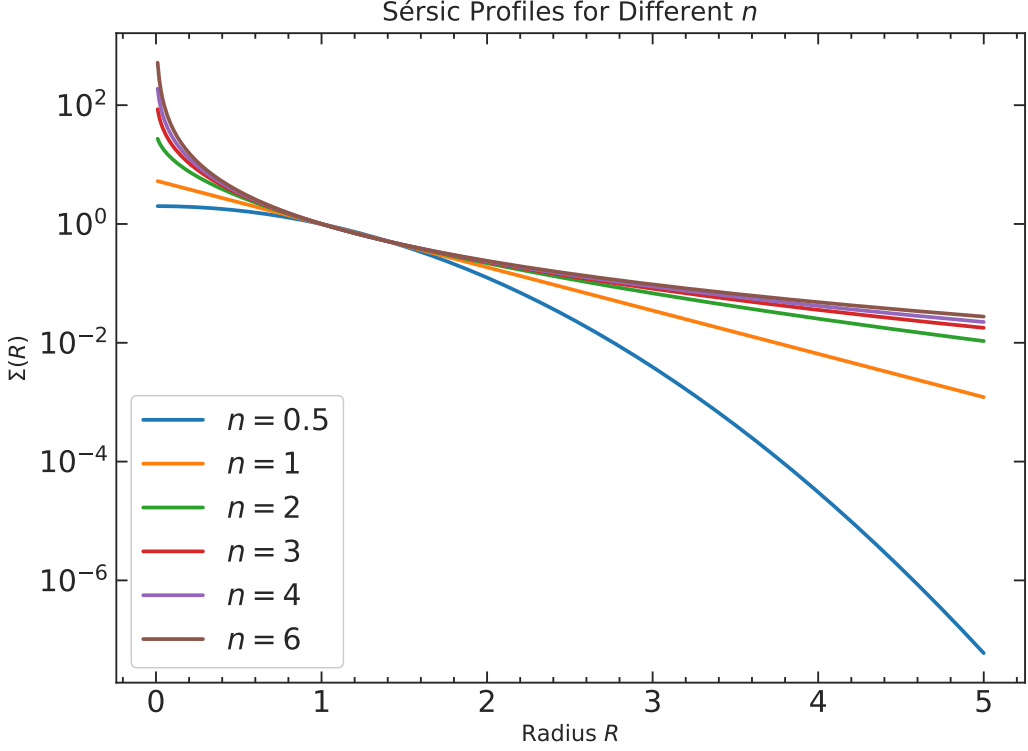


Figure 10: Sérsic profile for a given central surface density Σ_0 and half-mass radius R_e and different values of the Sérsic index n

3.2 Fitting

The surface density of the galaxy is fit by a pure sersic profile, a pure exponential profile and a combination of both. The combined profile is given by equation 4. The profiles are fit in log scale and the fitting process returns the optimized parameters $\Sigma(R_e)_{bulge}$, $\Sigma_{0,disc}$, R_e , R_d and n to minimize the residuals between the model and the observed data in log-space.

$$\Sigma(R) = \Sigma(R_e)_{bulge} \exp \left[-\beta_n \left\{ \left(\frac{R}{R_e} \right)^{1/n} - 1 \right\} \right] + \Sigma_{0,disc} \exp \left(\frac{-R}{R_d} \right) \quad (4)$$

To calculate the surface density profile of the galaxy as a function of the galactocentric radius, I first project the positions of the stars onto a plane perpendicular to the angular momentum(11). For a star orbiting on the disc plane, its angular momentum is directed upwards. Initially, I computed each galaxy's bulk angular momentum using all its star particles. Subsequently, I restricted this calculation to stars within a spherical radius of $3R_e$. This choice ensures that the effect of any poorly resolved source at the outskirts, a satellite galaxy or other fly-by objects which can significantly alter the rotation of the galaxy, is removed.

The projected vectors on the plane can be calculated using simple vector transformation

$$\vec{r}_{alongL} = (\vec{r} \cdot \hat{l})\hat{l} \quad (5)$$

where $\hat{l} = \frac{\vec{L}}{||\vec{L}||}$ is the unit vector along angular momentum vector. The projection of the vector on the plane of the disc is then

$$\vec{r}_{proj} = \vec{r} - (\vec{r} \cdot \hat{l})\hat{l} \quad (6)$$

The projected vectors are now binned into concentric annular bins in linear scale (refer figure 12). I allow the binning to extend from the 35pc, which is the size of one cell in the simulation, to a maximum of 1.5 times their radius enclosing 95% of the mass (hereon, referred to as R_{95}). I bin it linearly into adequate number of bins so that each bin has a width greater than the size of one cell in the simulation. Initially, I employed a binning with around 500 bins for the same limit which resulted in a profile with very few number of stars per bin, which led to an unreliable fit. I then reduced the number of bins appropriately.

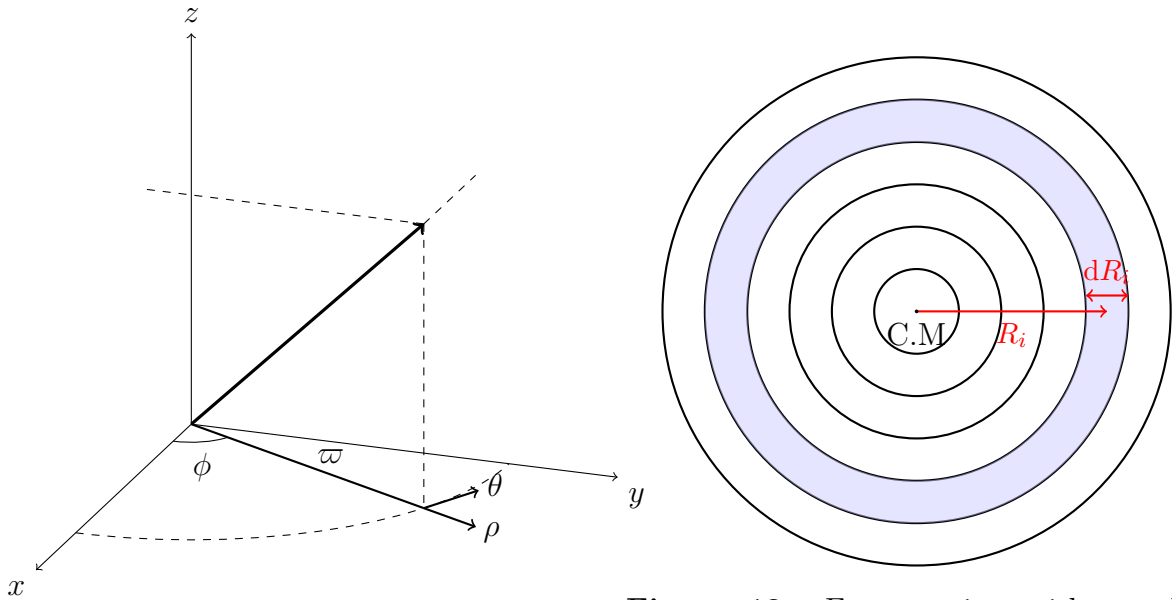


Figure 11: Projection of a star onto the galactic disk (in the $\hat{\rho}$ - $\hat{\theta}$ plane).

Figure 12: Face-on view with annular bins; the highlighted ring is used for computing $\Sigma(R_i)$.

The surface density $\Sigma(R_i)$ for the i -th annulus of central radius R_i width dR_i is calculated as

$$\Sigma(R_i) = \frac{1}{2\pi R_i dR_i} \sum_{j \in \text{annulus } i} m_j \quad (7)$$

where m_j is the mass of the j -th star in the i -th annulus and dR_i is the width of the i -th annulus. Since the binning is done in linear scale, the width of every bin remains the same. R_i denotes the central radius of the i -th annulus (refer figure 12). For the fitting, I utilized the `scipy.optimize.curve_fit` function from the SciPy library to perform a non-linear least squares fitting of our surface density profile $\Sigma(R)$ with the profile given by equation 4

Evaluation of the adequacy of the fit is important to understand how the data deviates from the model. The goodness of the fit is determined by calculating the χ^2 value of the fitting. Specifically, the data consists of measurements of surface density profiles binned by radius where each bin consists of N_i number of stars. This serves as a weighting factor reflecting the statistical significance of each bin.

$$\chi^2 = \frac{1}{\text{dof}} \sum_i N_i (y_{\text{data},i} - y_{\text{model},i})^2 \quad (8)$$

where dof is the degree of freedom which is often the number of free parameters and can be simplified as dof = n - p where n is the number of data points and p is the number of fitted parameters in the model. Weighting the residuals by N_i accounts for the fact that bins with more stars provide more statistically robust estimates and should thus contribute more strongly to the goodness-of-fit metric. Dividing by the degrees of freedom normalizes the variance, allowing for comparison across different models and datasets. Since variance is a measure of the discrepancy between the model and the data, the lower values would indicate a better fit.

3.3 Determination of mass fractions

The total stellar mass of a galaxy is obtained by integrating the surface density profiles over galactocentric radius R. For a given surface density profile, the total mass M is calculated as

$$M = 2\pi \int_0^\infty \Sigma(R) R dR \quad (9)$$

The stellar mass of a galaxy that consists of a bulge and a disc component can be written as

$$M_{\text{gal}} = M_{\text{bulge}} + M_{\text{disc}} \quad (10)$$

where

$$M_{\text{bulge}} = 2\pi \int_0^\infty \Sigma_{\text{bulge}}(R) R dR \quad (11)$$

$$M_{\text{disc}} = 2\pi \int_0^\infty \Sigma_{\text{disc}}(R) R dR \quad (12)$$

The mass fractions of the bulge and the disc, referred to as the bulge-to-total (B/T) and disc-to-total (D/T) ratio is then

$$B/T = \frac{M_{\text{bulge}}}{M_{\text{bulge}} + M_{\text{disc}}} \quad (13)$$

$$D/T = \frac{M_{\text{disc}}}{M_{\text{bulge}} + M_{\text{disc}}} \quad (14)$$

These ratios give the relative contributions of the spheroidal and the disc component to the total mass of the galaxy.

3.4 Kinematic analysis

To complement the distribution of stellar mass in determining the morphology of the galaxy, analyzing its kinematic composition is essential. By doing a kinematic analysis, we try to assess the rotational support of galaxies in the sample. Thus, analyzing the kinematic composition involved measuring rotation curves, velocity dispersions and distinguish rotation-dominated regions from dispersion dominated bulges. For this, I measure the rotation-to-dispersion ratio (V/σ) of every galaxy to assess the dominance of ordered rotation versus random motions.

I now compute the vector components of velocity vector in the cylindrical coordinate system to calculate the orbital velocity component. A velocity vector in this coordinate system can be expressed as

$$\vec{v} = v_\rho \hat{\rho} + v_\theta \hat{\theta} + v_l \hat{l} \quad (15)$$

Therefore,

$$v_{rot} = \vec{v} \cdot \hat{\theta} \quad (16)$$

The velocity dispersion of each velocity component—measured relative to its mean value along the basis vectors are denoted by σ_ρ , σ_θ and σ_l . It measures the spread in velocities of stars or gas orbiting within galaxy. An approximation for a one dimensional velocity dispersion that accounts for motion in the three directions is given by

$$\sigma = \sqrt{\frac{\sigma_\rho^2 + \sigma_\theta^2 + \sigma_l^2}{3}} \quad (17)$$

3.4.1 Computing the rotation curve

To analyze the orbital velocity of stars, we divide the galaxy into concentric annular bins as shown in figure 12. Within each radial bin, the mass-weighted mean of all three velocity components ($v_{\theta,i}$, $v_{r,i}$, $v_{l,i}$) and dispersion components ($\sigma_{\theta,i}$, $\sigma_{r,i}$, $\sigma_{l,i}$) are calculated as per equations 18-23. m_i is the total mass of stars in the i-th bin. This averaging accounts for the contribution of each particle's mass to the overall rotational motion.

$$\langle v_\theta \rangle(R) = \frac{\sum_{i \in R} m_i v_{\theta,i}}{\sum_{i \in R} m_i} \quad (18)$$

$$\langle v_r \rangle(R) = \frac{\sum_{i \in R} m_i v_{r,i}}{\sum_{i \in R} m_i} \quad (19)$$

$$\langle v_l \rangle(R) = \frac{\sum_{i \in R} m_i v_{l,i}}{\sum_{i \in R} m_i} \quad (20)$$

$$\sigma_r^2(R) = \frac{\sum_{i \in R} m_i (v_{r,i} - \langle v_r \rangle(R))^2}{\sum_{i \in R} m_i} \quad (21)$$

$$\sigma_\theta^2(R) = \frac{\sum_{i \in R} m_i (v_{\theta,i} - \langle v_\theta \rangle(R))^2}{\sum_{i \in R} m_i} \quad (22)$$

$$\sigma_l^2(R) = \frac{\sum_{i \in R} m_i (v_{l,i} - \langle v_l \rangle(R))^2}{\sum_{i \in R} m_i} \quad (23)$$

Using the obtained values the rotational velocity, dispersion and the rotation-to-dispersion ratio as a function of the distance from the axis of rotation is studied. From the rotation curve and dispersion profile, I compute V/σ values for all galaxies at different radii. I calculate the V/σ ratio at four different radii: R_{50} , R_d , $2.16R_d$ and R_{95} . These radii are chosen to represent different regions of the galaxy, with R_{50} being the radius enclosing half of the total stellar mass, R_d being the disc scale length, $2.16R_d$ being the radius at which the rotation curve peaks for a purely exponential disc and R_{95} being the radius enclosing 95% of the total stellar mass.

4 Results

In this chapter, I present a detailed analysis of the galaxies in the selected sample, with the aim of characterizing their physical structure and dynamical state. The results are organized into two main sections: the first examines the morphological properties of galaxies, such as surface density profiles and structural components, while the second investigates their kinematic features, including rotation curves and velocity dispersion profiles. The morphological analysis emphasizes the spatial distribution of stars in the galaxy, while the kinematic study evaluates rotational support and dispersion to classify galaxies dynamically.

4.1 Morphological profiling

As discussed in the previous chapter, I fit the surface density profiles of galaxies with a two-component model consisting of a Sersic + exponential profile and single component models which are pure Sersic profile fitting at inner radii and pure exponential profile fitting at larger radii. This fitting procedure yielded the best-fit parameters for both bulge and disc components. These parameters allow the calculation of mass fractions and provide insight into the concentration of spatial extent of the spheroidal and disc components as the comparisons across galaxies can reveal trends in structural evolution. Figure 13 shows fitting of stellar surface density profiles of galaxy 14215 with $R_{exp} = 0.33\text{kpc}$, $R_{sersic} = 0.0645\text{kpc}$ and $n=1.009$.

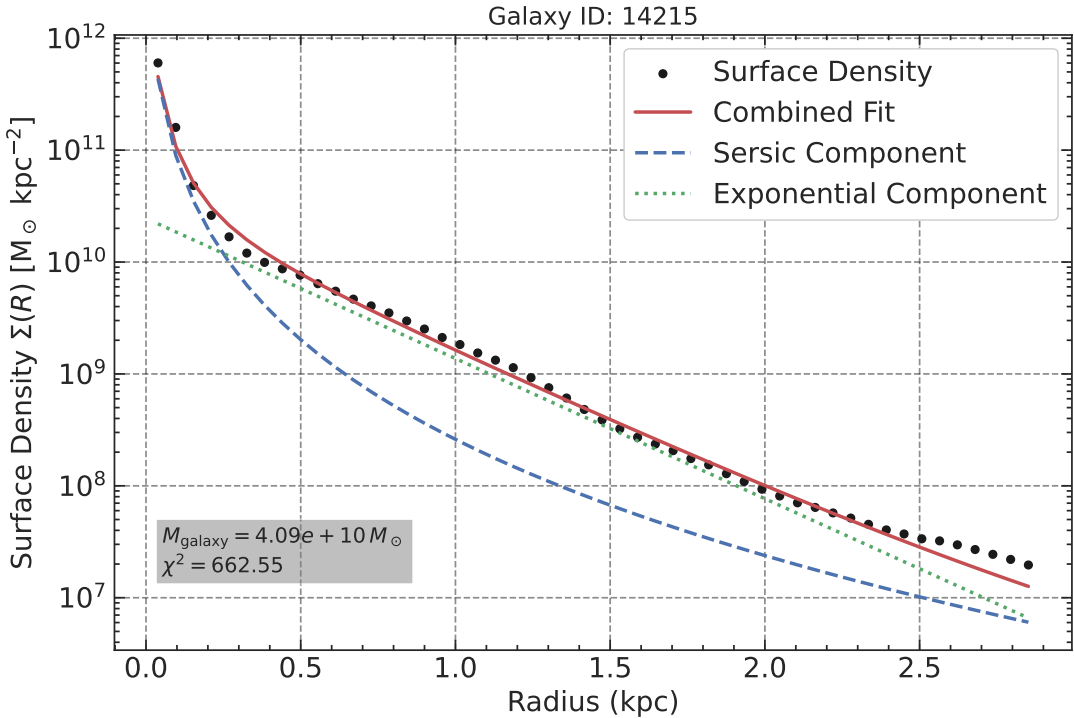


Figure 13: Surface density profile fit for the most massive galaxy in the sample. The black points represent the observed surface density profile, while the solid red line shows the best 2-component fit. The dashed blue line represents the Sersic component of the combined fit, whereas the dotted green line represents that of the exponential component.

The effective radius of the Sersic component in equation 4 would be referred to as R_{sersic} and that of the exponential component as R_{exp} . For galaxies with pure exponential profile, this R_{exp} becomes the disc scale length of the galaxy.

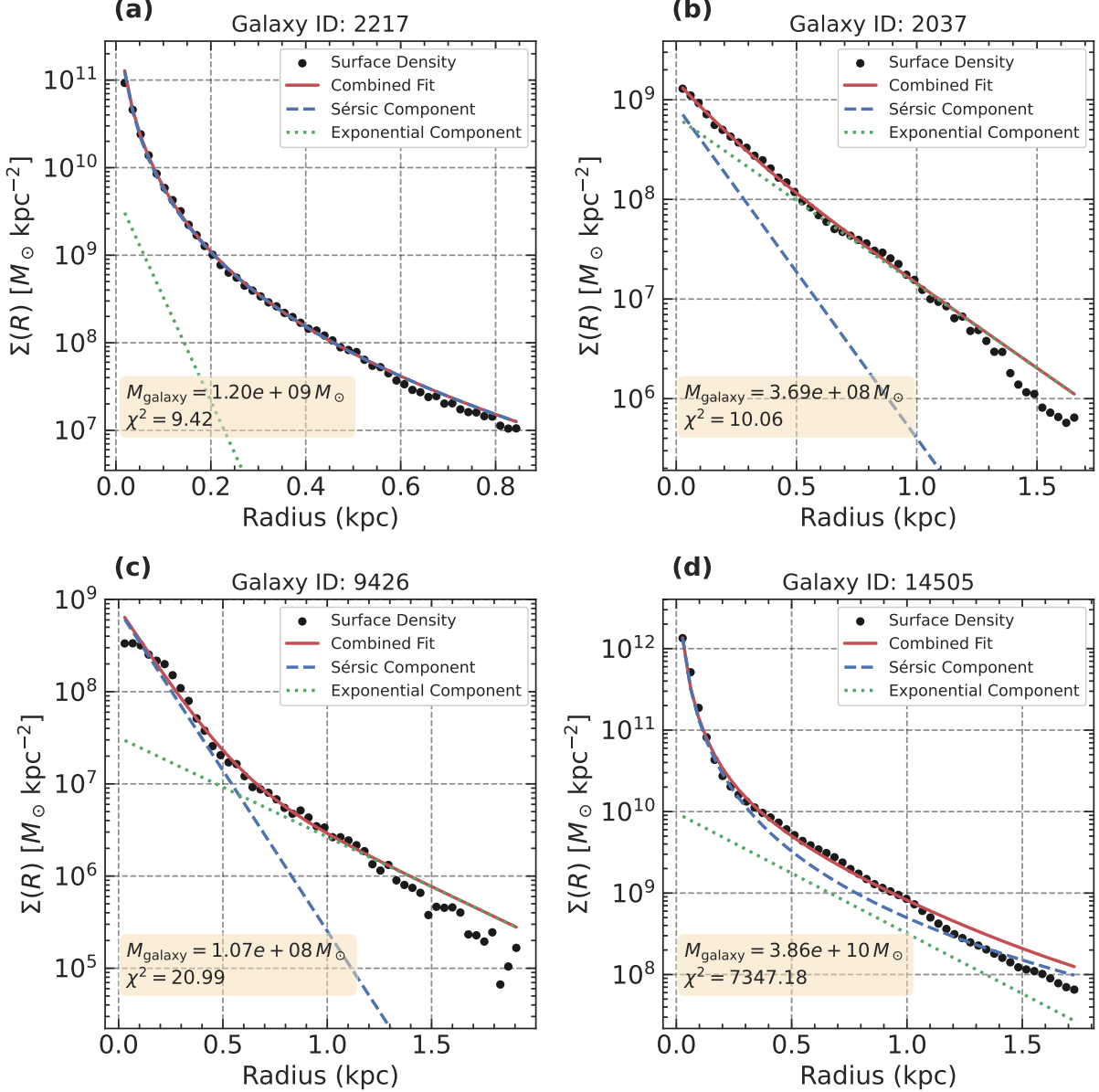


Figure 14: Surface density profile fit for 4 galaxies in the sample. The galaxies are so chosen as to represent the different structural types. The points and lines are same as in figure 13

Galaxies in the sample exhibit a wide range of profiles. The galaxies can be categorized into different structural types based on the best-fit model.

- **Pure sersic:** These galaxies are best fit by a single Sersic profile, indicating a spheroidal structure with a concentration of stars towards the center. Figure 14(a) follows such a profile, with $n = 3.05$ and no significant contribution from the exponential component. This can suggest a compact, spheroidal, bulge-dominated

structure, with no significant disc component. The effective radius R_e is about 0.037 kpc.

- **Pure exponential:** Such galaxies have a dominant exponential profile, with minor or no sersic contribution. In the sample, galaxy 14(b) is an example of this type, with a best-fit Sersic index $n = 1.0$ and a disc scale length $R_d \simeq 0.25$ kpc. This indicates a disc-like structure with a smooth, exponential decline in surface density.
- **Sersic + exponential:** The galaxies that are best fit by a combination of both profiles, is an indication of a more complex structure. In cases where the Sersic index is low ($n \simeq 1$), the galaxy represents two exponential discs (refer figure 14(c)). The best-fit exponential scale length for this galaxy is $R_d = 0.04$ kpc. Galaxies with a higher sersic index ($n \geq 2$) indicate a spheroidal inner component with a disc-like outer component. Figure 14(d) shows such a galaxy with $n = 6.3$.

We see that R_{sersic} of the galaxy fit by a pure Sersic profile is around 37pc, which is approximately the size of one cell in the simulation. This indicates that the Sersic component is not well resolved in this case. The Sersic index of the galaxy is also very high, which indicates a compact spheroidal structure. In the case of the galaxy fit by a perfect exponential profile (with no sersic contribution), the disc scale length R_d is around 250pc, that means that 50% of the mass is enclosed in a much larger radius from the center of mass of the galaxy. While in the former case, we have a very concentrated and compact distribution of stars near the central region (as scale length is as small as 37pc), in the latter, the mass is distributed in a much larger surface area, depicting an extended disc.

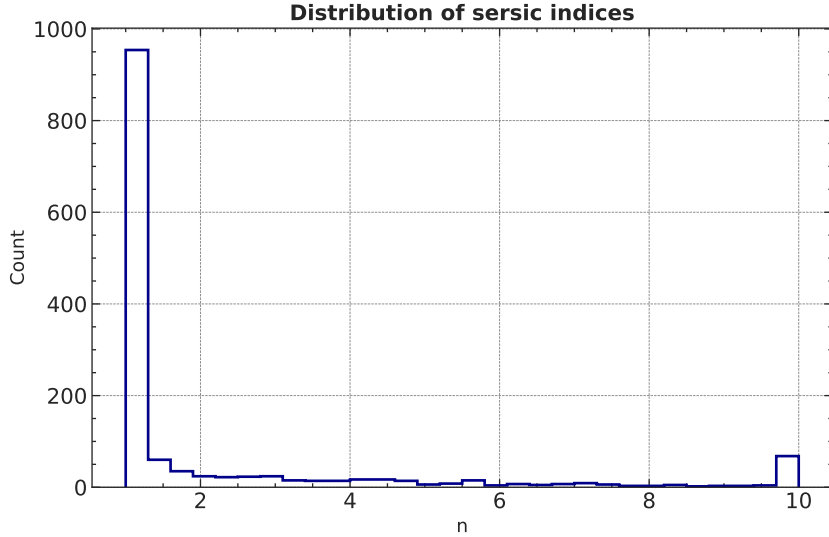


Figure 16: Distribution of Sersic index n for the galaxies in the sample. The histogram shows the number of galaxies with a given Sersic index, indicating a range of structural properties.

Figure 16 shows the distribution of estimated sersic indices of the combined profile fitting of galaxies in the sample. The distribution has a peak at $n \approx 1.0$, indicating that

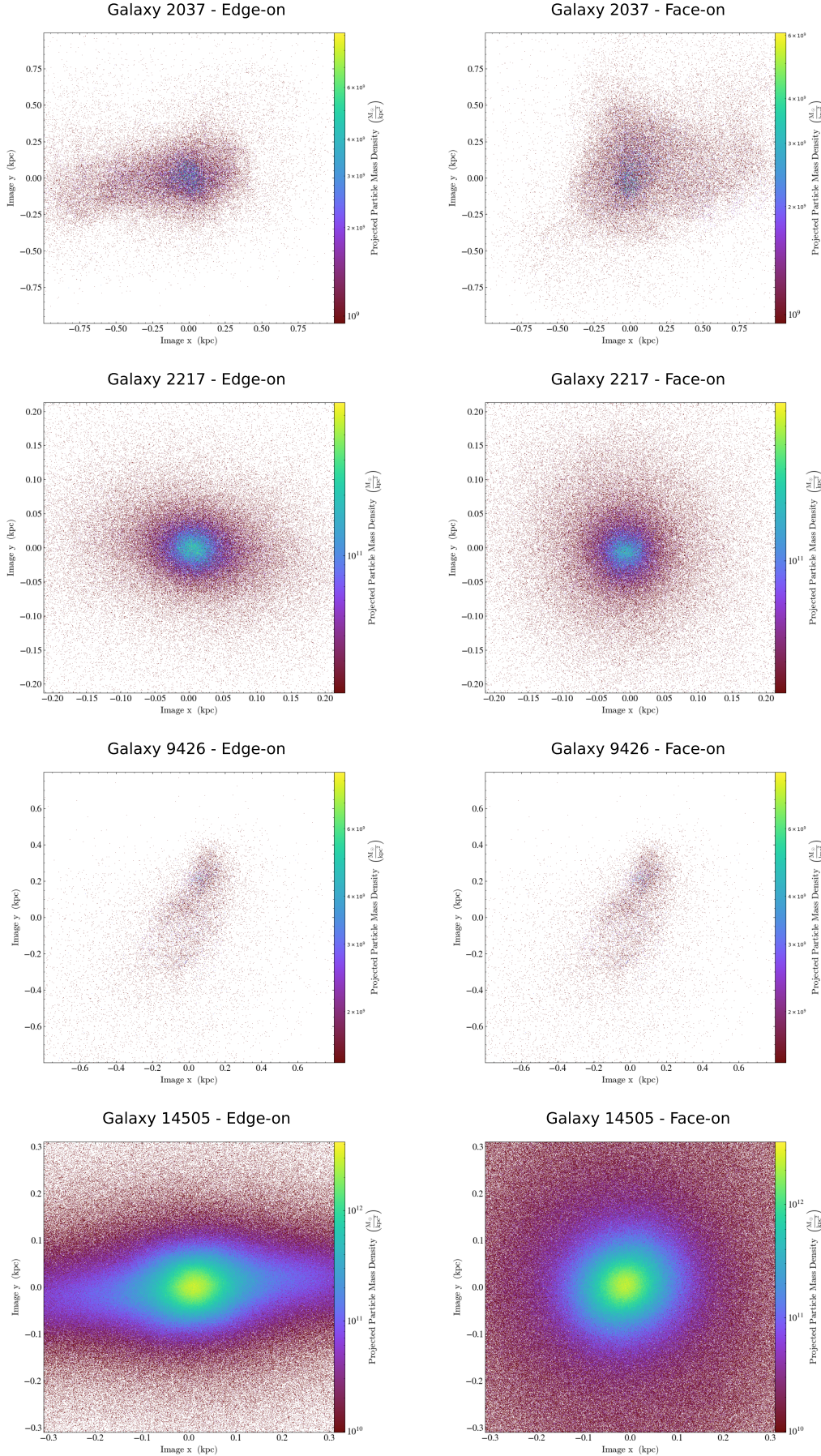


Figure 15: Stellar mapping for the galaxies whose surface density profiles are shown in figure 14

a large number of galaxies follow an exponential profile at the central part (The Sérsic component approximates to an exponential profile when $n=1$). The upper limit for the Sérsic index in the fitting procedure was fixed at $n=10$, which may explain the small peak observed in the distribution of galaxies. This likely reflects cases where the fitting algorithm reached the imposed boundary, rather than a true physical concentration at that value.

4.1.1 Mass fractions

The bulge-to-total ratio (B/T) and the disc-to-total ratio (D/T) determined are the mass contributions from the sersic and the exponential components respectively. Figure 17 shows the distribution of disk contribution to the total mass of the galaxy. Most of the galaxies with $M_* > 10^{10} M_\odot$ have a $D/T < 0.5$. 75% of the galaxies in the sample have a D/T ratio less than ~ 0.62 .

R_{exp} of galaxies in the sample extends to about 10kpc, with a very small D/T for galaxies with a compact central concentration, R_{sersic} .

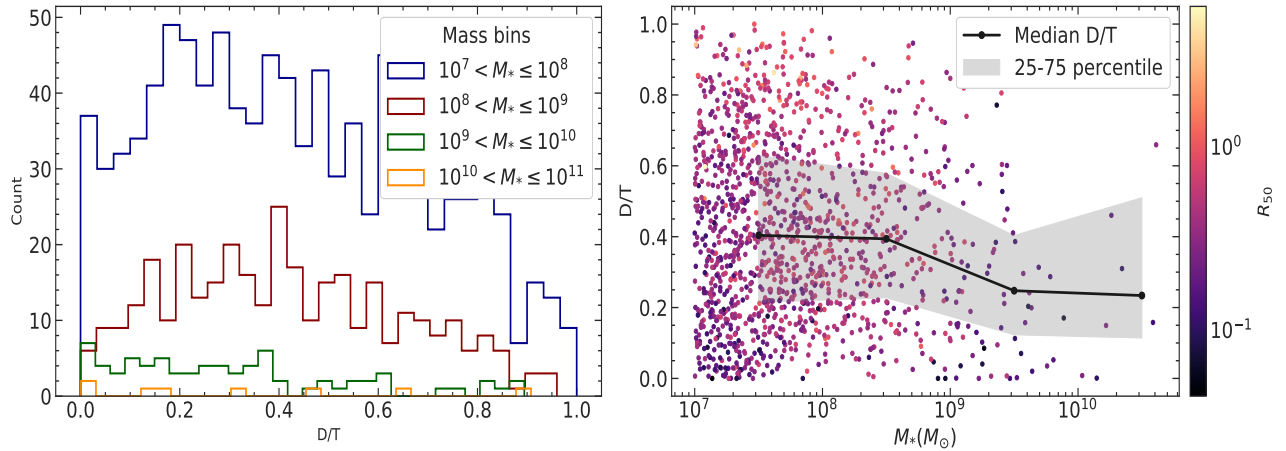


Figure 17: Distribution of disc-to-total ratio (D/T) for galaxies in the sample in each mass bin(left panel). The disc contribution to the total mass of the galaxy with increasing stellar mass(right panel). The shaded regions represent the 25th-75th percentile of the D/T distribution of galaxies. The median D/T value is shown as a solid line

Most galaxies with $D/T > 0.5$ ratios shows to have larger exponential scale lengths, indicating a more extended disc component (refer figure 18). Most galaxies in the sample lie in the mass range $10^7 M_\odot < M_* < 10^{8.5} M_\odot$, with a majority of them with an exponential scale length less than 1kpc.

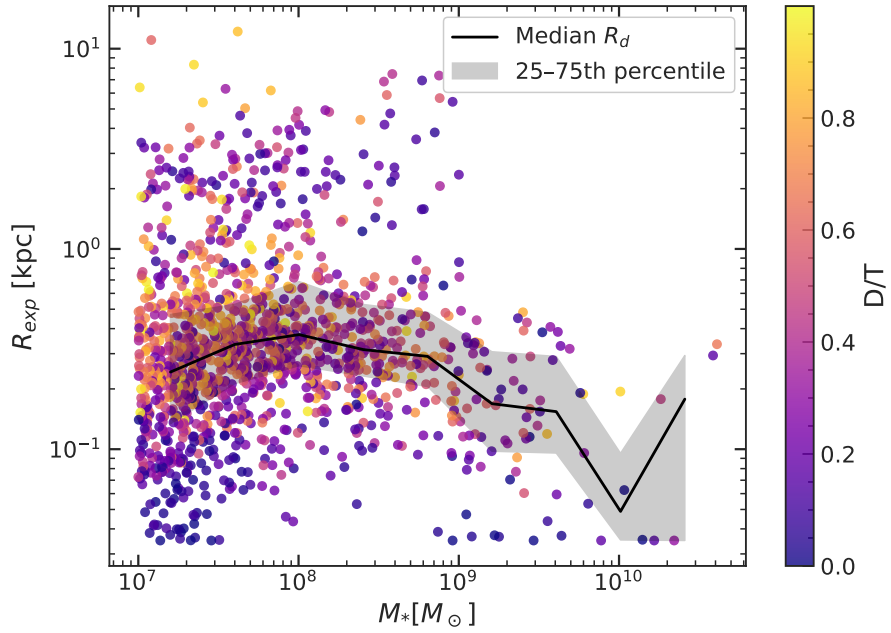


Figure 18: The exponential scale length R_{exp} of galaxies in the sample as a function of stellar mass M_* .

4.1.2 Sersic indices and scale lengths

From figure 19, it can be seen that some galaxies with a larger sersic scale length shows a high value of D/T. Essentially, the sersic indices of galaxies with a higher R_{sersic} has a distribution as given in figure 20a. This shows that a huge population of galaxies with $R_{exp} < R_{sersic}$ behaves like two-exponential discs (the central region following a Sersic profile with $n=1$). From equation 4, for $n \approx 1$, the scale length of the sersic component can be approximated as $R_s \approx 1.68R_e$, since $\beta_n = 2n - 0.324 \approx 1.68$ for $n = 1$.

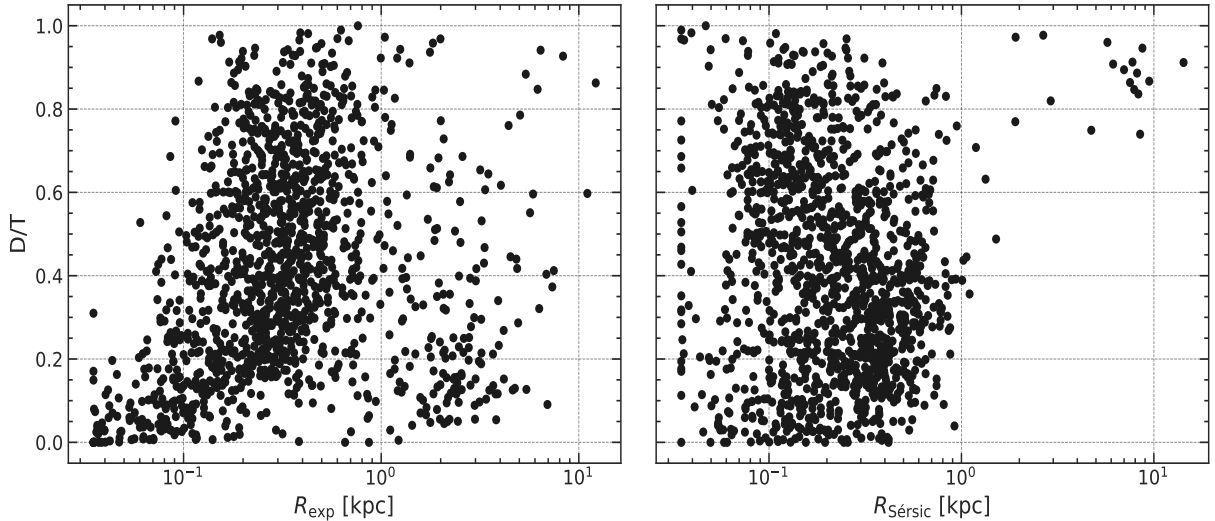
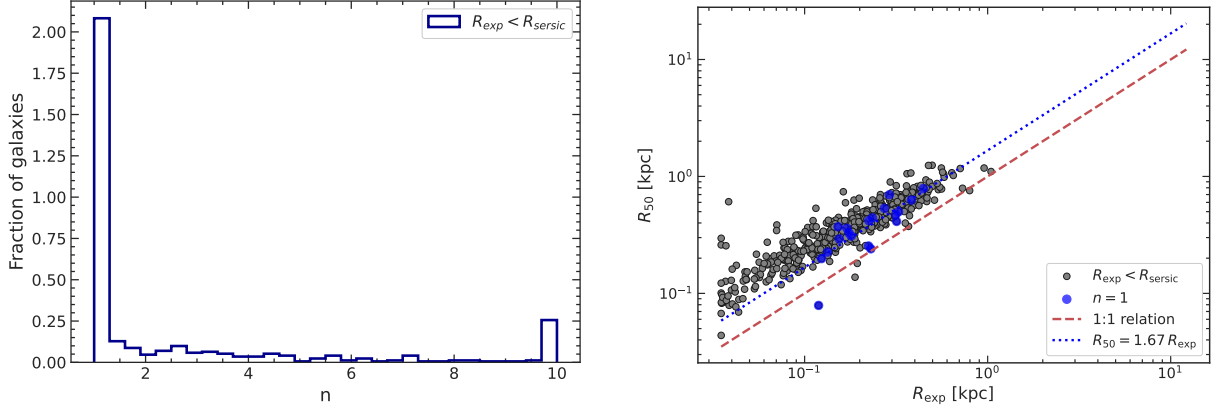


Figure 19: Scale length variation with disc-to-total ratio (D/T) for galaxies in the sample. The Sersic scale length of galaxies even with a higher D/T ratio is smaller than the exponential scale length.

Some galaxies have a larger Sersic scale length as compared to the exponential scale length with Sersic index =1. These galaxies exhibit shallow, exponential surface density profiles—lacking the steep central light excess typical of spheroidal bulges. The exponential scale length increases with half mass radius measured(refer figure 20b).As discussed before, the Sersic function reduces to an exponential profile with an exponential profile and a scale length $R_s \approx 1.68R_e$. Physcially this could mean that the smaller scale length in the fit corresponds to the inner-disk while the larger scale length traces the extended outer disk. Figure 21 compares the two scale lengths for such galaxies.



(a) Sersic index distribution of galaxies with $R_{exp} < R_{sersic}$

(b) Fig shows the relation between the exponential scale lengths and half mass radius with $R_{exp} < R_{sersic}$ and $n \approx 1$. We see that it is the same in case where $n=1$

Figure 20

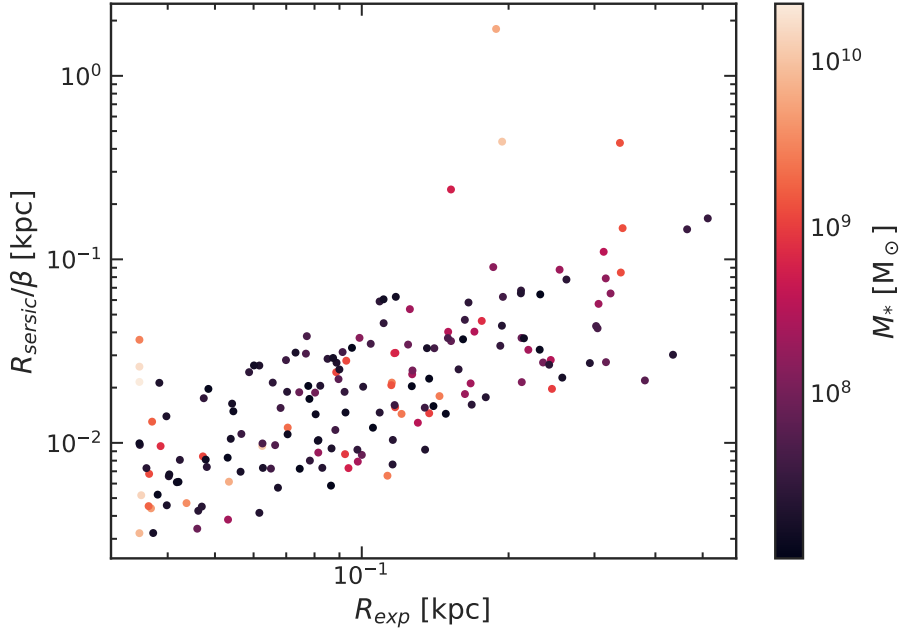


Figure 21: The "effective scale length" of the Sersic component for galaxies with $n \approx 1$ can be approximated to R_{sersic}/β

Figure 22 illustrates how the scale lengths compare to the radius enclosing 95% of the stellar mass providing insight into the structural extent of galaxies relative to their overall size. We see that for galaxies whose fraction of Sersic scale length to the total size of the galaxy is lesser than its corresponding exponential scale length, the disc contribution is also lower. I further explore how morphology relates to star formation activity of a galaxy. Star formation rate density (Σ_{SFR}), defined by $\Sigma_{SFR} = SFR/(2\pi R_e^2)$ is a measure of the rate at which stars are formed per unit area in a galaxy. Figure 23 shows the distribution of Σ_{SFR} with respect to the disc scale length R_{exp} . For a given SFR, Σ_{SFR} decreases with increasing effective radius.

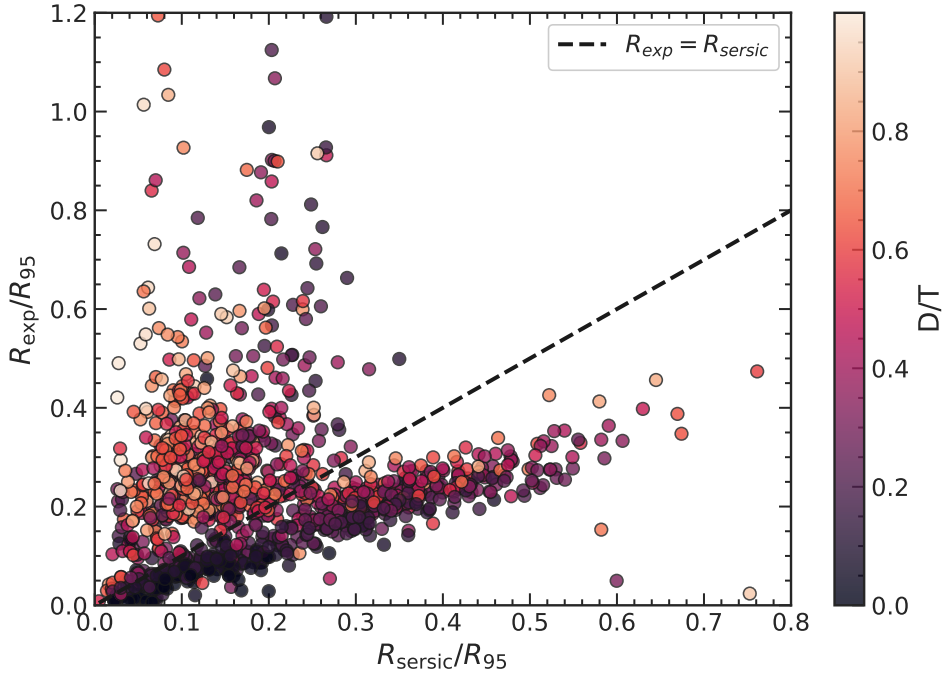


Figure 22: Fraction of Sersic scale length and exponential scale length to the R_{95} of the galaxy. The radius enclosing 95% of the stellar mass is a measure of the overall size of the galaxy

The morphological analysis reveals a diverse population of galaxy structures—from pure discs and double-exponential profiles to systems with distinct inner and outer components. However, these photometric decompositions alone cannot definitively uncover the underlying dynamical state of each object. As shown by various studies (eg., Thob et al. [2019]), galaxies with similar morphologies can exhibit a wide range of kinematic behaviors—such as rotation-dominated or dispersion-supported systems—and vice versa. Therefore, a comprehensive understanding of galaxy morphology requires integrating both photometric and kinematic analyses, like velocity fields, rotation curves and dispersion maps. This motivates the next section, where we transition to a detailed kinematic analysis of these galaxies, to classify them dynamically.

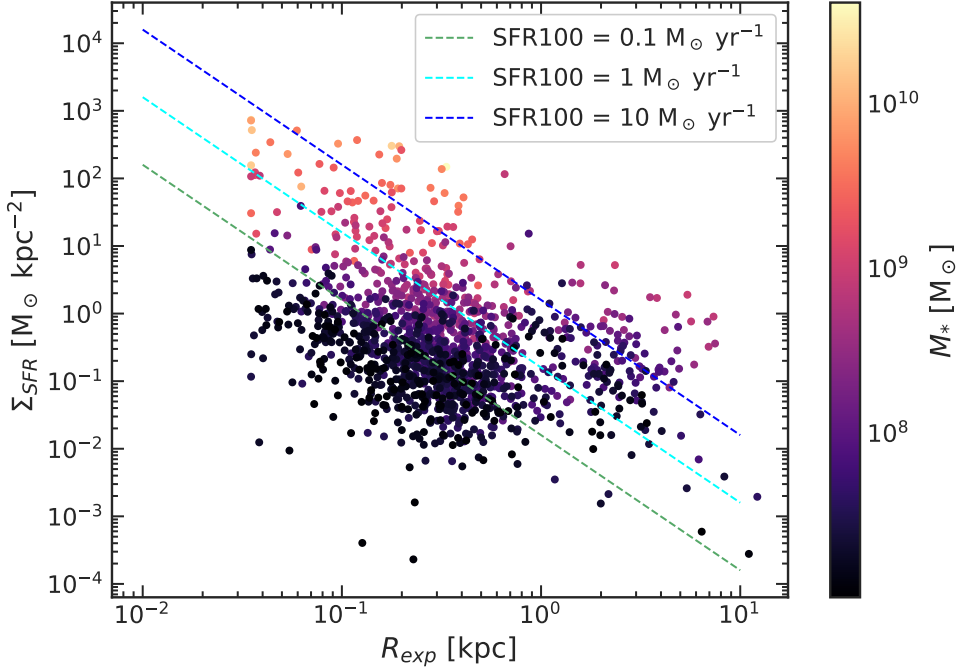


Figure 23: The star formation rate density (Σ_{SFR}) as a function of the disc scale length R_{exp} . The dotted line represents the star formation rate density for a galaxy with a given SFR

4.2 Kinematic analysis

The kinematic analysis of galaxies gives a deeper understanding of their dynamical state. In this section, I present the kinematic analysis of galaxies in the sample and try to see if it is in good agreement with the expected structural properties.

4.2.1 Rotation curves

This section presents the findings of the rotation-to-dispersion ratio (V/σ) computed as a function of the distance from the axis of rotation, computed from the orbital velocity and 3D dispersion of stars at each point. Figure 24 shows the rotation curves of galaxies in the sample. At the central region, the dispersion dominates. The rotation-to-dispersion ratio is computed as a function of radial distance R , as seen in figure 25. The V/σ measurements at R_{50} , exponential scale length R_d , $2.16R_d$ and R_{95} are further correlated to the morphological findings of this study. In some galaxies, the measured $V_\theta(R)$ becomes negative at certain radii, indicating counter-rotating stars.

For pure exponential discs, the rotation curve peaks at $2.16R_d$, where the rotation is dominated by the disc component. The V/σ ratio at this radius is expected to be greater than 1, indicating a disc-like structure. However, this is not always the case in my sample. As we saw in the previous section, many of these galaxies do not exhibit a pure exponential surface density profile; instead, their stellar distributions can include significant contributions from bulge-like or spheroidal components, which affect the gravitational potential and shift the rotation curve peak away from the theoretical expectation.

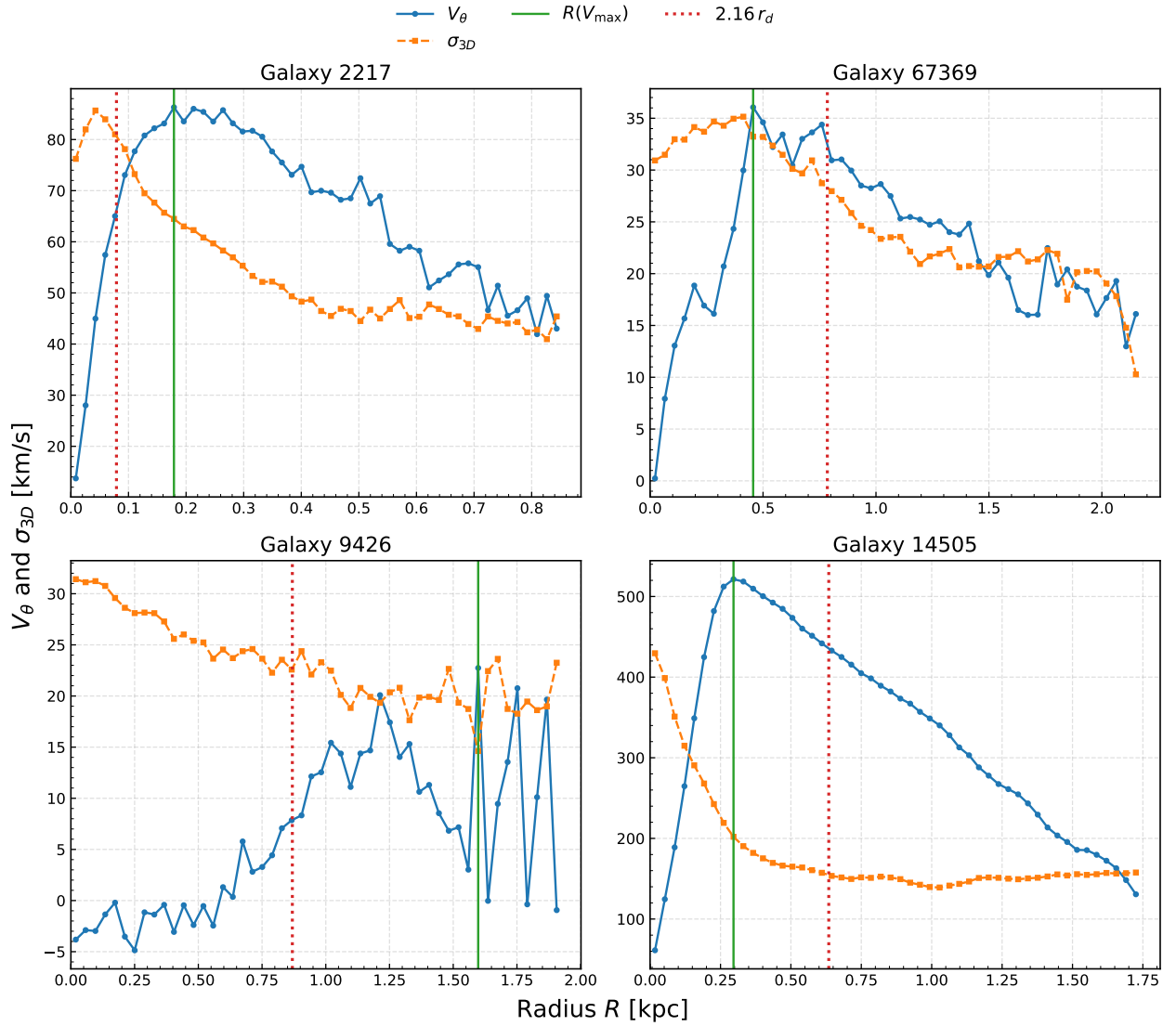


Figure 24: Rotation curves of galaxies in the sample

We see from the above figure that the peak of the rotation curve is not always at $2.16 * R_d$, which is expected for a pure exponential disc. This is because many of the galaxies in the sample are not pure exponential discs, but rather have a combination of bulge and disc components.

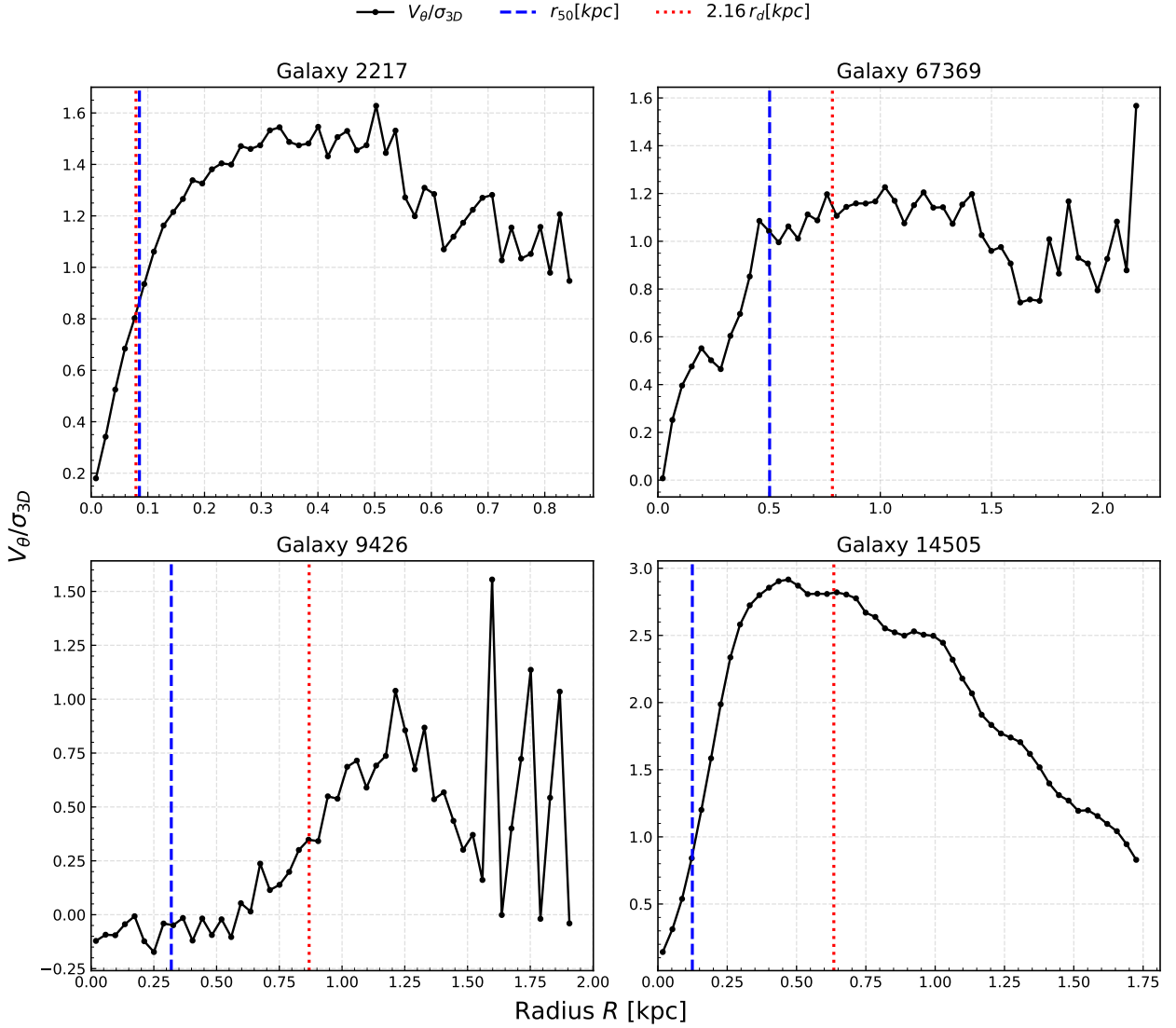


Figure 25: The rotation-to-dispersion ratio (V/σ) as a function of distance from the center of mass of the galaxy

4.2.2 Correlating with morphological profiles and galaxy properties

The observed V/σ value at the radii, shows an increase with the stellar mass of the galaxy (refer figure 26). This trend suggests that more massive galaxies tend to have higher rotational support. This is consistent with the expectation that more massive galaxies have deeper gravitational potentials, leading to higher rotational velocities.

The V/σ at each radii probes different dynamical regions of the galaxy. At R_{50} , the V/σ values takes into account the combined influence of the disk and any central mass concentrations and that at R_{exp} would take into account the influence of the disk component. A more meaningful comparison can be made at $2.16R_d$, which is theoretically the radius at which the the rotational velocity is expected to peak for a self-gravitating, pure exponential disc. The V/σ at this radius is expected to be greater than 1, indicating a disc-like structure. I also compute the ratio at R_{95} , which can characterize the outer regions of

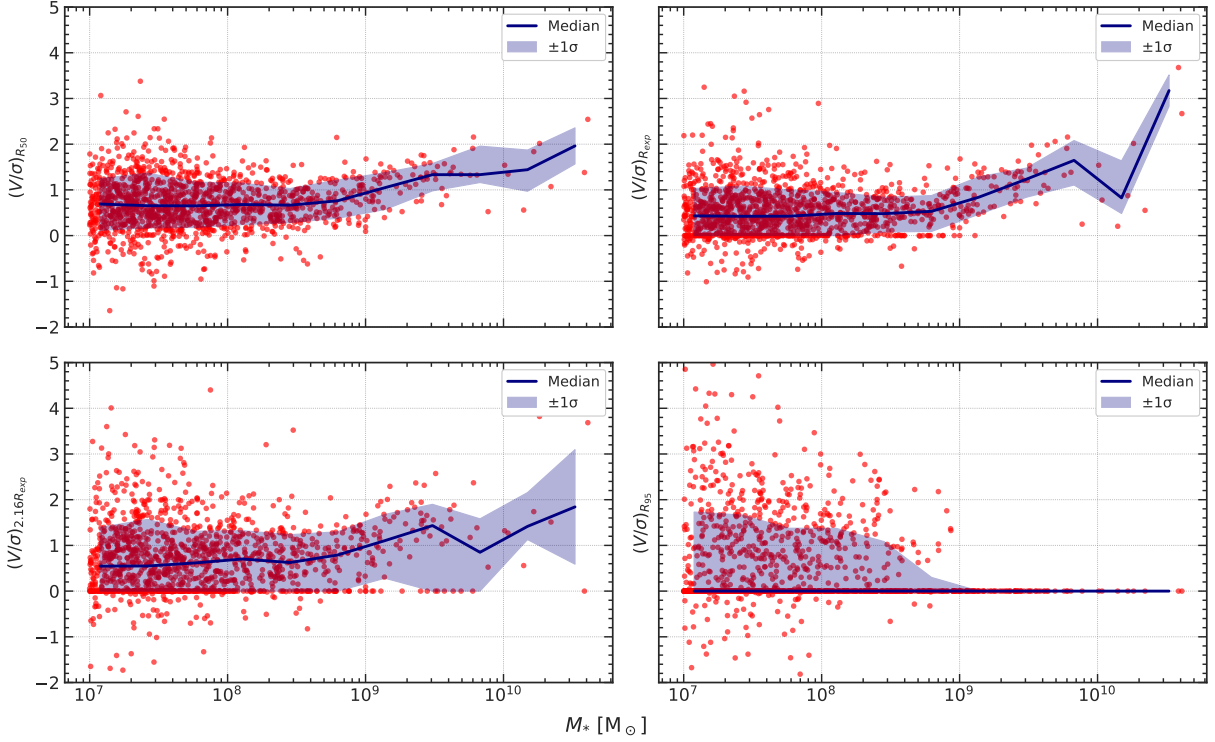


Figure 26: Variation of the rotation-to-dispersion ratio (V/σ) at R_{50} with stellar mass of galaxies in the sample. The shaded region represents a 1σ scatter

the galaxy, which is prone to interactions or accretion. In my study, I utilize all the four measurements to bring a bigger picture.

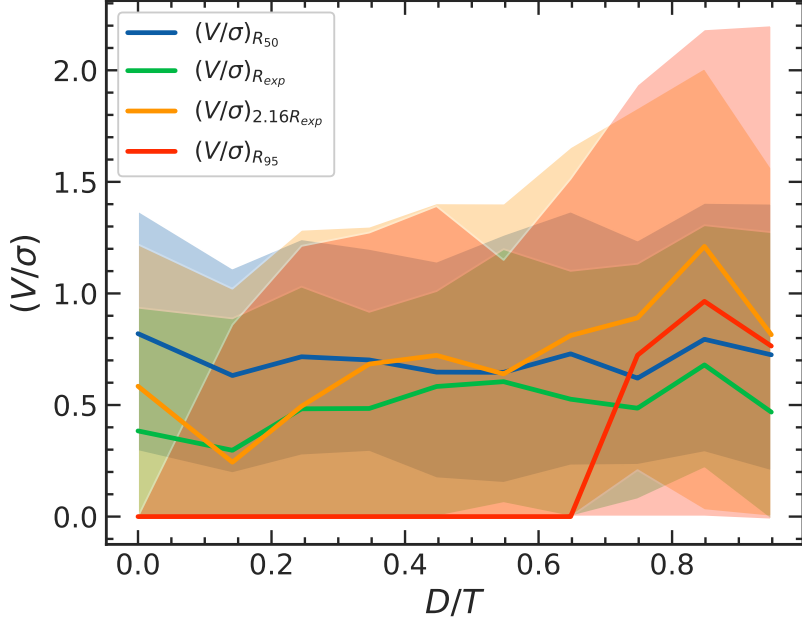


Figure 27: The V/σ at different radii as a function of D/T . The solid line represents the median value of V/σ at each D/T bin, while the shaded region represents the 1σ scatter

In the sample, the V/σ at R_{50} shows a good correlation with the D/T ratio, as shown

in figure 27. The galaxies with a higher D/T ratio shows a higher V/σ at these radii. The V/σ at R_{95} does not show a significant correlation with the D/T ratio.

5 Discussion

The kinematic analysis of galaxies in the sample reveals a complex interplay between morphology and dynamics. In my study, I find galaxies with a wide range of structural properties. The morphological analysis shows the presence of galaxies with a predominant spheroidal component, an extended disc component and galaxies with a concentrated central bulge with an outer disc. Galaxies identified towards the lower mass end, have a clump of stars enclosed in a small radius, indicating a compact structure without an extended disc. From the fitting, we saw that the half-mass radius of galaxies well fit by the exponential profile ($n=1$) is much larger than that of galaxies with a pure Sersic profile ($n \gg 1$). This is a good indication of the reliability of the bulge+disc fitting procedure.

The fitting, done using `scipy.optimize.curve_fit`, can be sensitive to the initial guesses of the parameters and bounds specified. While this does not drastically alter the results, it is important to note the potential biases introduced by the choice of initial parameters. For my work, I have tried fitting with various bound limits to see how the observed values are changing.

Complementing the morphological analysis, the kinematic analysis provides information about the dynamical state of these galaxies. From our study, we saw that there is (an average) increase in the V/σ ratio with the disc-to-total ratio. One thing that can be noted is that the number of galaxies above $10^{10} M_\odot$ are much less in number compared to other mass bins in the data. While the sample is not large enough to draw strong conclusions, it does suggest that more massive galaxies tend to have higher rotational support. The V/σ values at R_{50} and $2.16R_d$ show a good correlation with the D/T ratio, indicating that galaxies with a higher disc contribution tend to have higher rotational support. This is consistent with the expectation that more massive galaxies have deeper gravitational potentials, leading to higher rotational velocities.

6 Future work

The analysis presented in this work provides a comprehensive understanding of the morphological and kinematic properties of galaxies in the sample. However, to further enhance the understanding of galactic morphology, a few additional steps can be taken. A detailed kinematic decomposition can be performed to separate the contributions of the bulge and disc components to the overall kinematics. Furthermore, the morphological profiling and kinematic decomposition can be employed on gas particles, to differentiate between warm and cold discs and to understand further the rotational support of galaxies at high redshift. Lastly, a comparison of the simulation model to observational evidences can be done to further bridge the gap between simulations and observations.

References

- Oscar Agertz, Romain Teyssier, and Ben Moore. The formation of disc galaxies in a Λ CDM universe. *Monthly Notices of the Royal Astronomical Society*, 410(2):1391–1408, January 2011. doi: 10.1111/j.1365-2966.2010.17530.x.
- Paul D. Allen, Simon P. Driver, Alister W. Graham, Ewan Cameron, Jochen Liske, and Roberto De Propris. The millennium galaxy catalogue: bulge-disc decomposition of 10095 nearby galaxies: Mgc: bulge-disc decomposition. *Monthly Notices of the Royal Astronomical Society*, 371(1):2–18, August 2006. ISSN 1365-2966. doi: 10.1111/j.1365-2966.2006.10586.x. URL <http://dx.doi.org/10.1111/j.1365-2966.2006.10586.x>.
- E. Athanassoula and I. Martinez-Valpuesta. Formation and evolution of bulges, 2007. URL <https://arxiv.org/abs/0710.1518>.
- D. Aubert, C. Pichon, and S. Colombi. The origin and implications of dark matter anisotropic cosmic infall on $\approx l_*$ haloes. *Monthly Notices of the Royal Astronomical Society*, 352(2):376–398, August 2004. ISSN 1365-2966. doi: 10.1111/j.1365-2966.2004.07883.x. URL <http://dx.doi.org/10.1111/j.1365-2966.2004.07883.x>.
- Frederic Bournaud, Bruce G. Elmegreen, and Debra Meloy Elmegreen. Rapid formation of exponential disks and bulges at high redshift from the dynamical evolution of clump-cluster and chain galaxies. *The Astrophysical Journal*, 670(1):237–248, November 2007. ISSN 1538-4357. doi: 10.1086/522077. URL <http://dx.doi.org/10.1086/522077>.
- A. Lola Danhaive, Sandro Tacchella, Hannah Übler, Anna de Graaff, Eiichi Egami, Benjamin D. Johnson, Fengwu Sun, Santiago Arribas, Andrew J. Bunker, Stefano Carniani, Gareth C. Jones, Roberto Maiolino, William McClymont, Eleonora Parlanti, Charlotte Simmonds, Natalia C. Villanueva, William M. Baker, Daniel T. Jaffe, Daniel Eisenstein, Kevin Hainline, Jakob M. Helton, Zhiyuan Ji, Xiaojing Lin, Dávid Puskás, Marcia Rieke, Pierluigi Rinaldi, Brant Robertson, Jan Scholz, Christina C. Williams, and Christopher N. A. Willmer. The dawn of disks: unveiling the turbulent ionised gas kinematics of the galaxy population at $z \sim 4 - 6$ with jwst/nircam grism spectroscopy, 2025. URL <https://arxiv.org/abs/2503.21863>.
- Gerard de Vaucouleurs. Recherches sur les Nebuleuses Extragalactiques. *Annales d'Astrophysique*, 11:247, January 1948.
- Yohan Dubois, Sébastien Peirani, Christophe Pichon, Julien Devriendt, Raphaël Gavazzi, Charlotte Welker, and Marta Volonteri. The horizon-agn simulation: morphological diversity of galaxies promoted by agn feedback. *Monthly Notices of the Royal Astronomical Society*, 463(4):3948–3964, September 2016. ISSN 1365-2966. doi: 10.1093/mnras/stw2265. URL <http://dx.doi.org/10.1093/mnras/stw2265>.
- S. M. Fall and G. Efstathiou. Formation and rotation of disc galaxies with haloes. *Monthly Notices of the Royal Astronomical Society*, 193:189–206, October 1980. doi: 10.1093/mnras/193.2.189.

Fan Fang and William C. Saslaw. Effects of galaxy mergers on their spatial distribution and luminosity function. *The Astrophysical Journal*, 476:534–543, February 1997. doi: 10.1086/303638. URL <https://iopscience.iop.org/article/10.1086/303638>. Received 1996 Mar 11; accepted 1996 Sep 6.

Leonardo Ferreira, Nathan Adams, Christopher J. Conselice, Elizaveta Sazonova, Duncan Austin, Joseph Caruana, Fabricio Ferrari, Aprajita Verma, James Trussler, Tom Broadhurst, Jose Diego, Brenda L. Frye, Massimo Pascale, Stephen M. Wilkins, Rogier A. Windhorst, and Adi Zitrin. Panic! at the disks: First rest-frame optical observations of galaxy structure at $z < 3$ with jwst in the smacs 0723 field. *The Astrophysical Journal Letters*, 938(1):L2, October 2022. ISSN 2041-8213. doi: 10.3847/2041-8213/ac947c. URL <http://dx.doi.org/10.3847/2041-8213/ac947c>.

Leonardo Ferreira, Christopher J. Conselice, Elizaveta Sazonova, Fabricio Ferrari, Joseph Caruana, Clár-Bríd Tohill, Geferson Lucatelli, Nathan Adams, Dimitrios Irodou, Madeline A. Marshall, Will J. Roper, Christopher C. Lovell, Aprajita Verma, Duncan Austin, James Trussler, and Stephen M. Wilkins. The jwst hubble sequence: The rest-frame optical evolution of galaxy structure at $1.5 < z < 6.5$. *The Astrophysical Journal*, 955(2):94, September 2023. ISSN 1538-4357. doi: 10.3847/1538-4357/acec76. URL <http://dx.doi.org/10.3847/1538-4357/acec76>.

K.C. Freeman. On the Disks of Spiral and S0 Galaxies. *Astrophysical Journal*, 160:811, June 1970. doi: 10.1086/150474.

F. Governato, C. Brook, L. Mayer, A. Brooks, G. Rhee, J. Wadsley, P. Jonsson, B. Willman, G. Stinson, T. Quinn, and P. Madau. Bulgeless dwarf galaxies and dark matter cores from supernova-driven outflows. *Nature*, 463(7278):203–206, January 2010. doi: 10.1038/nature08640.

Alister W. Graham and Simon P. Driver. A concise reference to (projected) sérsic $r_{1/n}$ quantities, including concentration, profile slopes, petrosian indices, and kron magnitudes. *Publications of the Astronomical Society of Australia*, 22(2):118–127, 2005. ISSN 1448-6083. doi: 10.1071/as05001. URL <http://dx.doi.org/10.1071/AS05001>.

Alexander B Gurvich, Jonathan Stern, Claude-André Faucher-Giguère, Philip F Hopkins, Andrew Wetzel, Jorge Moreno, Christopher C Hayward, Alexander J Richings, and Zachary Hafen. Rapid disc settling and the transition from bursty to steady star formation in milky way-mass galaxies. *Monthly Notices of the Royal Astronomical Society*, 519(2):2598–2614, December 2022. ISSN 1365-2966. doi: 10.1093/mnras/stac3712. URL <http://dx.doi.org/10.1093/mnras/stac3712>.

E. P. Hubble. Extragalactic nebulae. *Astrophysical Journal*, 64:321–369, December 1926. doi: 10.1086/143018.

E. Komatsu, K. M. Smith, J. Dunkley, C. L. Bennett, B. Gold, G. Hinshaw, N. Jarosik, D. Larson, M. R. Nolta, L. Page, D. N. Spergel, M. Halpern, R. S. Hill, A. Kogut, M. Limon, S. S. Meyer, N. Odegard, G. S. Tucker, J. L. Weiland, E. Wollack, and

- E. L. Wright. Seven-year wilkinson microwave anisotropy probe(wmap) observations: Cosmological interpretation. *The Astrophysical Journal Supplement Series*, 192(2):18, January 2011. ISSN 1538-4365. doi: 10.1088/0067-0049/192/2/18. URL <http://dx.doi.org/10.1088/0067-0049/192/2/18>.
- J. Kormendy. A morphological survey of bar, lens, and ring components in galaxies: secular evolution in galaxy structure. *Astrophysical Journal*, 227:714–728, February 1979. doi: 10.1086/156782.
- John Kormendy and Robert C. Kennicutt. Secular evolution and the formation of pseudobulges in disk galaxies. *Annual Review of Astronomy and Astrophysics*, 42(1):603–683, September 2004. ISSN 1545-4282. doi: 10.1146/annurev.astro.42.053102.134024. URL <http://dx.doi.org/10.1146/annurev.astro.42.053102.134024>.
- O. Le Fèvre, M. Béthermin, A. Faisst, G. C. Jones, P. Capak, P. Cassata, J. D. Silverman, D. Schaefer, L. Yan, R. Amorin, S. Bardelli, M. Boquien, A. Cimatti, M. Dessauges-Zavadsky, M. Giavalisco, N. P. Hathi, Y. Fudamoto, S. Fujimoto, M. Ginolfi, C. Gruppioni, S. Hemmati, E. Ibar, A. Koekemoer, Y. Khushanova, G. Lagache, B. C. Lemaux, F. Loiacono, R. Maiolino, C. Mancini, D. Narayanan, L. Morselli, Hugo Méndez-Hernández, P. A. Oesch, F. Pozzi, M. Romano, D. Riechers, N. Scoville, M. Talia, L. A. M. Tasca, R. Thomas, S. Toft, L. Vallini, D. Vergani, F. Walter, G. Zamorani, and E. Zucca. The alpine-alma [cii] survey: Survey strategy, observations, and sample properties of 118 star-forming galaxies at $4 < z < 6$. *Astronomy and Astrophysics*, 643:A1, October 2020. ISSN 1432-0746. doi: 10.1051/0004-6361/201936965. URL <http://dx.doi.org/10.1051/0004-6361/201936965>.
- Houjun Mo, Frank C. van den Bosch, and Simon White. *Galaxy Formation and Evolution*. Cambridge University Press, Cambridge, UK, 1st edition, 2010. ISBN 9780521857932. doi: 10.1017/CBO9780511807244. URL <https://doi.org/10.1017/CBO9780511807244>.
- Julio F. Navarro and Matthias Steinmetz. Dark halo and disk galaxy scaling laws in hierarchical universes. *The Astrophysical Journal*, 538(2):477–488, August 2000. ISSN 1538-4357. doi: 10.1086/309175. URL <http://dx.doi.org/10.1086/309175>.
- Kalina V Nedkova, Boris Häufler, Danilo Marchesini, Gabriel B Brammer, Adina D Feinstein, Evelyn J Johnston, Jeyhan S Kartaltepe, Anton M Koekemoer, Nicholas S Martis, Adam Muzzin, Marc Rafelski, Heath V Shipley, Rosalind E Skelton, Mauro Stefanon, Arjen van der Wel, and Katherine E Whitaker. Bulge+disc decomposition of hff and candels galaxies: Uvj diagrams and stellar mass-size relations of galaxy components at $0.2 \geq z \geq 1.5$. *Monthly Notices of the Royal Astronomical Society*, 532(4):3747–3777, 07 2024. ISSN 0035-8711. doi: 10.1093/mnras/stae1702. URL <https://doi.org/10.1093/mnras/stae1702>.
- Erica June Nelson, Pieter G. van Dokkum, Ivelina Momcheva, Gabriel Brammer, Britt Lundgren, Rosalind E. Skelton, Katherine E. Whitaker, Elisabete Da Cunha, Natascha Förster Schreiber, Marijn Franx, Mattia Fumagalli, Mariska Kriek, Ivo Labbe, Joel

- Leja, Shannon Patel, Hans-Walter Rix, Kasper B. Schmidt, Arjen van der Wel, and Stijn Wuyts. The radial distribution of star formation in galaxies at $z \sim 1$ from the 3d-hst survey. *The Astrophysical Journal*, 763(1):L16, January 2013. ISSN 2041-8213. doi: 10.1088/2041-8205/763/1/l16. URL <http://dx.doi.org/10.1088/2041-8205/763/1/L16>.
- E. Parlanti, S. Carniani, A. Pallottini, M. Cignoni, G. Cresci, M. Kohandel, F. Mannucci, and A. Marconi. Alma hints at the presence of turbulent disk galaxies at $z > 5$. *Astronomy and Astrophysics*, 673:A153, May 2023. ISSN 1432-0746. doi: 10.1051/0004-6361/202245603. URL <http://dx.doi.org/10.1051/0004-6361/202245603>.
- Annalisa Pillepich, Dylan Nelson, Volker Springel, Rüdiger Pakmor, Paul Torrey, Rainer Weinberger, Mark Vogelsberger, Federico Marinacci, Shy Genel, Arjen van der Wel, and Lars Hernquist. First results from the tng50 simulation: the evolution of stellar and gaseous discs across cosmic time. *Monthly Notices of the Royal Astronomical Society*, 490(3):3196–3233, September 2019. ISSN 1365-2966. doi: 10.1093/mnras/stz2338. URL <http://dx.doi.org/10.1093/mnras/stz2338>.
- L. Quilley, V. de Lapparent, M. Baes, M. Bolzonella, I. Damjanov, B. Häußler, F. R. Marleau, A. Nervesian, T. Saifollahi, D. Scott, J. G. Sorce, C. Tortora, M. Urbano, N. Aghanim, B. Altieri, A. Amara, S. Andreon, N. Auricchio, C. Baccigalupi, M. Baldi, A. Balestra, S. Bardelli, A. Bassett, P. Battaglia, A. Biviano, A. Bonchi, D. Bonino, E. Branchini, M. Brescia, J. Brinchmann, A. Caillat, S. Camera, V. Capobianco, C. Carbone, J. Carretero, S. Casas, M. Castellano, G. Castignani, S. Cavuoti, A. Cimatti, C. Colodro-Conde, G. Congedo, C. J. Conselice, L. Conversi, Y. Copin, F. Courbin, H. M. Courtois, M. Cropper, J. C. Cuillandre, A. Da Silva, H. Degaudenzi, G. De Lucia, A. M. Di Giorgio, J. Dinis, F. Dubath, C. A. J. Duncan, X. Dupac, S. Dusini, A. Ealet, M. Farina, S. Farrens, F. Faustini, S. Ferriol, S. Fotopoulou, M. Frailis, E. Franceschi, M. Fumana, S. Galeotta, K. George, B. Gillis, C. Giocoli, P. Gómez-Alvarez, A. Grazian, F. Grupp, S. V. H. Haugan, J. Hoar, W. Holmes, F. Hormuth, A. Hornstrup, P. Hudelot, K. Jahnke, M. Jhabvala, E. Keihänen, S. Keremiche, A. Kiessling, M. Kilbinger, B. Kubik, K. Kuijken, M. Kümmel, M. Kunz, H. Kurki-Suonio, R. Laureijs, D. Le Mignant, S. Ligori, P. B. Lilje, V. Lindholm, I. Lloro, G. Mainetti, D. Maino, E. Maiorano, O. Mansutti, O. Marggraf, K. Markovic, M. Martinelli, N. Martinet, F. Marulli, R. Massey, E. Medinaceli, S. Mei, M. Melchior, Y. Mellier, M. Meneghetti, E. Merlin, G. Meylan, A. Mora, M. Moresco, L. Moscardini, R. Nakajima, C. Neissner, R. C. Nichol, S. M. Niemi, C. Padilla, S. Paltani, F. Pasian, K. Pedersen, W. J. Percival, V. Pettorino, S. Pires, G. Polenta, M. Poncet, L. A. Popa, L. Pozzetti, F. Raison, R. Rebolo, A. Renzi, J. Rhodes, G. Riccio, E. Romelli, M. Roncarelli, E. Rossetti, R. Saglia, Z. Sakr, D. Sapone, B. Sartoris, M. Schirmer, P. Schneider, T. Schrabback, A. Secroun, E. Sefusatti, G. Seidel, S. Serrano, C. Sirignano, G. Sirri, L. Stanco, J. Steinwagner, P. Tallada-Crespí, A. N. Taylor, I. Tereno, R. Toledo-Moreo, F. Torradeflot, I. Tutusaus, L. Valenziano, T. Vassallo, G. Verdoes Kleijn, A. Veropalumbo, Y. Wang, J. Weller, G. Zamorani, E. Zucca, C. Burigana, and

- V. Scottez. Euclid: Galaxy morphology and photometry from bulge-disc decomposition of early release observations, 2025. URL <https://arxiv.org/abs/2502.15581>.
- Jian Ren, Nan Li, F. S. Liu, Qifan Cui, Mingxiang Fu, and Xian Zhong Zheng. Revisiting Galaxy Evolution in Morphology in the Cosmic Evolution Survey Field (COSMOS-ReGEM). I. Merging Galaxies. *Astrophysical Journal*, 958(1):96, November 2023. doi: 10.3847/1538-4357/acfee.
- Allan Sandage. *The Hubble Atlas of Galaxies*. 1961.
- J. L. Sérsic. Influence of the atmospheric and instrumental dispersion on the brightness distribution in a galaxy. *Boletin de la Asociacion Argentina de Astronomia La Plata Argentina*, 6:41–43, February 1963.
- Jose Luis Sersic. *Atlas de Galaxias Australes*. Observatorio Astronomico, Cordoba, Argentina, 1968.
- Joseph Silk and Martin J. Rees. Quasars and galaxy formation. *Astronomy & Astrophysics*, 331:L1–L4, March 1998. doi: 10.48550/arXiv.astro-ph/9801013.
- Renske Smit, Rychard J. Bouwens, Stefano Carniani, Pascal A. Oesch, Ivo Labb  , Garth D. Illingworth, Paul van der Werf, Larry D. Bradley, Valentino Gonzalez, Jacqueline A. Hodge, Benne W. Holwerda, Roberto Maiolino, and Wei Zheng. Rotation in [c ii]-emitting gas in two galaxies at a redshift of 6.8. *Nature*, 553(7687): 178–181, January 2018. ISSN 1476-4687. doi: 10.1038/nature24631. URL <http://dx.doi.org/10.1038/nature24631>.
- R. Teyssier. Cosmological hydrodynamics with adaptive mesh refinement: A new high resolution code called ramses. *Astronomy and Astrophysics*, 385(1):337–364, April 2002. ISSN 1432-0746. doi: 10.1051/0004-6361:20011817. URL <http://dx.doi.org/10.1051/0004-6361:20011817>.
- Adrien C R Thob, Robert A Crain, Ian G McCarthy, Matthieu Schaller, Claudia D P Lagos, Joop Schaye, Geert Jan J Talens, Philip A James, Tom Theuns, and Richard G Bower. The relationship between the morphology and kinematics of galaxies and its dependence on dark matter halo structure in eagle. *Monthly Notices of the Royal Astronomical Society*, 485(1):972–987, February 2019. ISSN 1365-2966. doi: 10.1093/mnras/stz448. URL <http://dx.doi.org/10.1093/mnras/stz448>.
- A. Toomre. On the gravitational stability of a disk of stars. *Astrophysical Journal*, 139: 1217–1238, May 1964. doi: 10.1086/147861.
- Alar Toomre. Mergers and Some Consequences. In Beatrice M. Tinsley and Richard B. Gehret Larson, D. Campbell, editors, *Evolution of Galaxies and Stellar Populations*, page 401, January 1977.

- Maxime Trebitsch, Yohan Dubois, Marta Volonteri, Hugo Pfister, Corentin Cadiou, Harley Katz, Joakim Rosdahl, Taysun Kimm, Christophe Pichon, Ricarda S. Beckmann, Julien Devriendt, and Adrianne Slyz. The obelisk simulation: Galaxies contribute more than agn to hi reionization of protoclusters. *Astronomy and Astrophysics*, 653:A154, September 2021. ISSN 1432-0746. doi: 10.1051/0004-6361/202037698. URL <http://dx.doi.org/10.1051/0004-6361/202037698>.
- D. Tweed, J. Devriendt, J. Blaizot, S. Colombi, and A. Slyz. Building merger trees from cosmologicaln-body simulations: Towards improving galaxy formation models using subhaloes. *Astronomy and Astrophysics*, 506(2):647–660, August 2009. ISSN 1432-0746. doi: 10.1051/0004-6361/200911787. URL <http://dx.doi.org/10.1051/0004-6361/200911787>.
- P.C. van der Kruit and K.C. Freeman. Galaxy disks. *Annual Review of Astronomy and Astrophysics*, 49(1):301–371, September 2011. ISSN 1545-4282. doi: 10.1146/annurev-astro-083109-153241. URL <http://dx.doi.org/10.1146/annurev-astro-083109-153241>.
- M. Volonteri, M. Trebitsch, J. E. Greene, Y. Dubois, C.-A. Dong-Paez, M. Habouzit, A. Lupi, Y. Ma, R. S. Beckmann, P. Dayal, and R. Schneider. Exploring active galactic nuclei and little red dots with the obelisk simulation. *Astronomy and Astrophysics*, 695:A33, February 2025. ISSN 1432-0746. doi: 10.1051/0004-6361/202451963. URL <http://dx.doi.org/10.1051/0004-6361/202451963>.
- S. D. M. White and M. J. Rees. Core condensation in heavy halos: a two-stage theory for galaxy formation and clustering. *Monthly Notices of the Royal Astronomical Society*, 183(3):341–358, 07 1978. ISSN 0035-8711. doi: 10.1093/mnras/183.3.341. URL <https://doi.org/10.1093/mnras/183.3.341>.
- E. Wisnioski, N. M. Förster Schreiber, M. Fossati, J. T. Mendel, D. Wilman, R. Genzel, R. Bender, S. Wuyts, R. L. Davies, H. Übler, K. Bandara, A. Beifiori, S. Belli, G. Brammer, J. Chan, M. Fabricius, P. Lang, E. J. Nelson, I. Momcheva, D. Rosario, R. Saglia, S. Seitz, L. J. Tacconi, and P. G. van Dokkum. The kmos3d survey: Data release and final survey paper. *The Astrophysical Journal*, 886(2):124, 2019. doi: 10.3847/1538-4357/ab4db8.